1   Revision 2

2

3   **Structural and spectroscopic study of the kieserite-dwornikite solid solution series,**

4   **(Mg,Ni)SO$_4$·H$_2$O, at ambient and low temperatures, with cosmochemical implications**

5   **for icy moons and Mars**

6
7

8   Dominik Talla[a*], Madeleine Balla[a], Claudia Aicher[a], Christian L. Lengauer[a], Manfred

9   Wildner[a]

10

11   [a]Institut für Mineralogie und Kristallographie, Althanstraße 14, 1090 Wien, Austria

12   *corresponding author

13

14

15

16   **Abstract**

17

18   The investigation of the presence and role of sulfates in our solar system receives

19   growing attention, as these compounds play a crucial role in the water budget of planets such

20   as Mars and significantly influence melting equilibria on the icy moons of Saturn and Jupiter,

21   leading to the formation of subsurface oceans and even cryovolcanism. Despite the dominant

22   presence of higher sulfate hydrates such as epsomite, MgSO$_4$·7H$_2$O, and mirabilite,

23   Na$_2$SO$_4$·10H$_2$O, on these moons' surfaces, it is not excluded that lower-hydrated sulfates,

24   such as kieserite, MgSO$_4$·H$_2$O, are also present, forming from higher hydrates under pressures

25   relevant to the mantle of the icy moons. Given the composition of the soluble fraction in C1

26   and C2 chondritic meteorites, which are high in Ni content and also considered to represent

27   the composition of the rocky cores of the Jovian icy moons, the actual compositions of

28   potentially present monohydrate sulfates likely lie at intermediate values along the solid

29   solution series between kieserite and transition-metal kieserite-group endmembers,

30   incorporating Ni in particular. Moderate Ni contents are also probable in kieserite on Mars

31   due to the planet's long-term accumulation of meteoritic nickel, although likely to a much

32   lesser extent than Fe.

33   Structural and spectroscopic differences between the pure Mg- and Ni-endmembers

34   have been previously documented in the literature, but no detailed crystal chemical and

35   spectroscopic investigation along the Mg-Ni solid solution has been done yet. The present

36   work proves the existence of a continuous $(Mg,Ni)SO_4 \cdot H_2O$ solid solution series for the first

37   time. It provides a detailed insight into the changes in lattice parameters, structural details and

38   positions of prominent bands in infrared (transmission, attenuated total reflectance, diffuse

39   reflectance) and Raman spectra in synthetic samples as the Ni/Mg ratio progresses, at both

40   ambient as well as low temperatures relevant for the icy moons and Mars. UV-Vis-NIR

41   crystal field spectra of the Ni endmember also help to elucidate the influence of Ni^{2+}-related

42   bands on the overtone- and combination modes.

43   The $(Mg,Ni)SO_4 \cdot H_2O$ solid solution series shows Vegard-type behavior, i.e. lattice

44   parameters as well as spectral band positions change along linear trends with increasing Ni

45   content. Infrared spectra reveal significant changes in the wavenumber positions of prominent

46   bands, depending on the Ni/Mg ratio. We show that also the temperature during measurement

47   has an influence on band position, mainly in case of H_2O-related bands. The changes

48   observed for several absorption features in the IR spectra enable rough estimation of the

49   Ni/Mg ratio in the monohydrate sulfate, which is applicable to present and future remote

50   sensing data, as well as in-situ measurements on Mars or the icy moons. The spectral features

51   most diagnostic of composition are the vibrational stretching modes of the H_2O molecule and

52   a band unique to kieserite-group compounds at around 900 cm^{-1} in the IR spectra, as well as

53   the pronounced v_3 and v_1 sulfate stretching modes visible in Raman spectra.

54

55   **Keywords:** Kieserite-dwornikite solid solution, icy satellites, Mars, crystal chemistry, FTIR

56   spectroscopy, Raman spectroscopy, UV-Vis-NIR spectroscopy

57

58

59

60

61   **Introduction**

62

63   The past few decades of planetary exploration uncovered the presence of considerable

64   amounts of sulfates in our solar system. From the surface (and subsurface) of Mars to the icy

65   moons of Jupiter and Saturn and even veinlets in chondritic meteorites, sulfates of Mg, Fe,

66   Mn and Ni represent an important constituent of planetary and meteoritic material

67   (Frederiksson and Kerridge 1988; Burgess et al. 1991; Kargel 1991). The existence of sulfate

68   deposits containing kieserite within layered terrains on Mars is now well established (e.g.,

69   Bishop et al. 2009; Noel et al. 2015; Mangold et al. 2008; Lichtenberg et al. 2010), most

70   probably as a solid solution between kieserite ($MgSO_4 \cdot H_2O$) and szomolnokite ($FeSO_4 \cdot H_2O$).

71   Minor Ni-contents are suggested by Papike et al. (2007), who note that Martian kieserite, via

72   partial Fe-, Ni-, or Co-incorporation, could be an indicator for meteorite impacts as relevant

73   processes in the formation and redistribution of sulfates on Mars. Moreover, Knauth et al.

74   (2005) suggest that the observed sulfate-cemented sedimentary structures could be ascribed to

75   impact surges from a large nickel-iron meteorite.

76   Hydrated Mg-sulfates as alteration products are known from C1 and C2 type

77   carbonaceous chondrites, making up to 73% by mass of their soluble fraction (Frederiksson

78   and Kerridge 1988; Burgess et al. 1991). The identification of higher-hydrated Na- and Mg-

79   sulfates on the surface of Jupiter's moons Ganymede and Europa is another important

80   discovery (McCord et al. 2001; Dalton et al. 2005, 2012). The formation of $MgSO_4$-H_2O-

81   Na_2SO_4 low-temperature eutectic brines is believed to be essential for the existence of crustal

82   rifting, cryovolcanism (both active and extinct), or the presence of subsurface oceans on

83   Jupiter's and Saturn's icy satellites (Kargel 1991; McCord et al. 2001). Such oceans could

84   theoretically sustain or have sustained extraterrestrial life in the past (Kargel et al. 2000;

85   McKinnon and Zolensky 2003; Spencer et al. 2009 and citations therein; Solomonidou et al.

86   2011). Active cryovolcanism, owing its existence to tidal heating, is now well documented

87   from the south-polar region of Saturn's moon Enceladus (Spencer et al. 2009). All of these

88   sulfates could have Ni substitution in their structures, and if they are monohydrated, their

89   composition could be identified with the research we present in this work.

90   The high sulfate hydration states interpreted to be present on the surface of icy moons

91   could be modified by interaction with cosmic radiation. For example, epsomite decomposes to

92   kieserite (Jamieson et al. 2014), the thermodynamic stability of which is strongly enhanced by

93   the surrounding vacuum (Zolotov and Shock 2001). The models of fractional eutectic melting

94   indicate the evolution of a Mg-sulfate precipitate ('salty ice') in the high-pressure ice mantle

95   region of the large icy satellites, potentially consisting also of lower sulfate hydrates (Kargel

96   1991; Nakamura and Ohtani 2011). Due to its higher buoyancy, this salty ice mixture is

97   believed to ascend upwards, supplying soluble salts to the overlying ocean (Journaux et al.

98   2017), thus providing nutrients for the potential evolution of extraterrestrial life (Vance et al.

99   2014). The basic stability of kieserite and isostructural sulfate monohydrates of transition

100 metals in such high-pressure environments, albeit modified by displacive second-order phase

101 transitions, is supported by recent investigations (Meusburger et al. 2018, 2019; Ende et al.

102 2019a,b).

103   The rocky cores of the icy moons of the gas giants, from which the salts now present in

104 their oceans and upper ice layers originated, probably correspond in composition to C1 or C2

105 chondritic material, containing sulfates of Mg, Mn and Ni in the soluble fraction (Burgess et

106 al. 1991; Kargel 1991). As such, the actual composition of monohydrated sulfate, should it be

107 present, will likely represent an intermediate value between kieserite ($MgSO_4 \cdot H_2O$) and its

108   isostructural transition-metal bearing compounds, in particular with Ni- and Mn-contents

109   (Frederiksson and Kerridge 1988, Anders and Grevese 1989).

110   Despite the knowledge of significant changes in lattice parameters and IR spectra

111   between kieserite and the Ni-endmember dwornikite (Wildner and Giester 1991; Stoilova and

112   Lutz 2002; Stoilova 2003), no detailed investigation of the structural and spectroscopic

113   behavior along the Mg-Ni solid solution series was done so far. A structural and crystal

114   chemical study was recently published by Bechtold and Wildner (2016) for the kieserite-

115   cobaltkieserite series, followed by a thorough examination including spectroscopic results of

116   the kieserite-szomolnokite solid solution, $Mg_{1-x}Fe_xSO_4 \cdot H_2O$, by Talla and Wildner (2019).

117   In this paper, we present the results of detailed structural, crystal chemical, Fourier

118   Transform Infrared (FTIR) and Raman-spectroscopic investigations on synthetically prepared

119   members along the binary kieserite-dwornikite solid solution, $Mg_{1-x}Ni_xSO_4 \cdot H_2O$, at ambient

120   and lower temperatures, as relevant for surface conditions of Mars and icy satellites of Jupiter

121   and Saturn, complemented by ultraviolet-visible-near infrared (UV-Vis-NIR) crystal field

122   spectra of Ni^{2+} in dwornikite. The presented data may prove valuable in further refining the

123   chemical composition of kieserite present on extraterrestrial bodies in our solar system based

124   on available remote sensing data in the mid-infrared range, as well as providing a fundamental

125   dataset for interpretation of future data of in-situ measurements by landers and rovers.

126   Note that throughout the present paper we use the name "dwornikite", originally

127   describing a mineral with approximate composition $(Ni_{0.9}Fe_{0.1})SO_4 \cdot H_2O$ (Milton et al. 1982),

128   to refer to the pure $NiSO_4 \cdot H_2O$ endmember.

129

130   **Experimental**

131

132   **Sample preparation**

133   The evaporation technique was used to prepare powder sample material for the IR and

134   Raman spectrocopic studies. Epsomite ($MgSO_4 \cdot 7H_2O$) was mixed with $NiSO_4 \cdot 6H_2O$ in the

135   desired Mg/Ni molar ratio, amounting to 6 g in total (both chemicals were of analytical

136   grade). The reagents were dissolved in a mixture of 80 ml of doubly distilled H_2O and 10 ml

137   95% H_2SO_4 in a beaker. The solution was evaporated at 70 °C for 10 days, yielding a crust of

138   pale green $(Mg,Ni)SO_4{\cdot}H_2O$ at the bottom of the vessel, covered by the remaining

139   concentrated acid. In addition, the following hydrothermal technique was used to synthesize

140   coarse-grained samples, enabling selection of individual single crystals for X-ray diffraction

141   and low-temperature Raman investigations. Teflon-lined stainless steel autoclaves with an

142   inner volume of ~2 cm^3 were filled with a mixture of epsomite $(MgSO_4{\cdot}7H_2O)$ and

143    $NiSO_4{\cdot}6H_2O$ amounting to 0.4 g in total with a pre-set Mg/Ni molar ratio. The solvent

144   consisted of 0.7 ml distilled H_2O and 2.2 ml concentrated H_2SO_4 (w = 0.95). All reagents

145   were of analytical grade. An isothermal temperature run at 220 °C for a period of 14 days

146   followed by cooling to room temperature within 4 days was used. Initial problems such as Ni

147   preferably remaining in solution, synthesized crystals of inadequate size and polysynthetic

148   twinning inherent to tightly sealed autoclaves (samples Ni5a to Ni40a), were largely resolved

149   by applying the 'leaking vessel approach'. A small leak between the Teflon reaction vessel

150   and its lid was allowed by only gently tightening the lid upon assembly. Through this leak,

151   H_2O slowly evaporated leading to slow precipitation of the monohydrate sulfates as an

152   aggregate of single crystals including individuals with sufficient quality and size.

153   Subsequent treatment of the product was the same for single crystals and powder

154   material as follows. After decanting the fluid and mechanical removal of the solids from the

155   reaction vessel, the product was rinsed twice with distilled H_2O, taking advantage of the

156   sulfate's relatively slow dissolution rate. Thereafter, the crystals were washed using 98%

157   ethanol to remove the H_2O from the previous step, and the product was dried in an oven at 65

158   °C overnight, then stored in airtight vials.

159

160   **Chemical analyses and powder X-ray diffraction**

161   Wet-chemical analyses were done on a part of each sample batch at the Masaryk

162   University in Brno, Czech Republic. An amount of ~0.5 g of ground sample material was

163   dissolved in boiling HNO_3 (w = 0.65). Contents of Mg and Ni were both determined

164   spectrophotometrically (instrument Solaar M5 - TJAsolutions, measurement time 4 s per

165   element) with an analytical error of 0.005 wt% for Mg and 0.002 wt% for Ni.

166   A further part of each sample batch was examined using powder X-ray diffraction, in

167   order to confirm expected lattice parameter shifts along the solid solution and the mono-phase

168   character of each batch. The material was pressed onto an Si-holder and measured on a

169   Philips PW 3710 diffractometer (measuring interval 5-120° 2Θ in 0.2° increments, measuring

170   time of 15 s per step). Following the phase identification with the program EVA2013,

171   Rietveld refinements were performed with the Bruker program TOPAS3.

172

173   **Single crystal X-ray diffraction**

174   Single crystals suitable for X-ray diffraction measurements were selected by choosing

175   individuals with homogeneous extinction under crossed polars. The crystal structures of ten

176   representatives along the $Mg_{1-x}Ni_xSO_4 \cdot H_2O$ solid solution series, including the dwornikite

177   endmember, were determined from diffraction data measured at 295 K with graphite-

178   monochromatized MoKα-radiation on a Nonius Kappa CCD diffractometer equipped with a

179   0.3 mm monocapillary X-ray optics collimator. Complete Ewald spheres up to 2θ = 80° were

180   each collected in several sets of φ- and ω-scans with 2° rotation per CCD frame, at a crystal to

181   detector distance of 30 mm. The integration and correction of the intensity data, including an

182   absorption correction by multi-frame scaling and the refinement of lattice parameters, were

183   done with the Nonius program DENZO-SMN.

184   Temperature-dependent X-ray data collections of the dwornikite endmember were

185   performed between +40 and −160 °C in steps of 40 K on a Bruker ApexII diffractometer

186   equipped with a CCD area detector and an Incoatec Microfocus Source IμS (30 W, multilayer

187   mirror, Mo-Kα radiation), in a dry stream of nitrogen (Cryostream 800, Oxford Cryosystems).

188   Several sets of φ- and ω-scans with 2° scan width were measured at a crystal-detector distance

189   of 40 mm up to 80° 2θ full sphere. Absorption was corrected by evaluation of multi-scans.

190   For the sake of data consistency, the lattice parameters extracted from the ApexII

191   temperature-dependent measurements were corrected in such a way that the interpolated

192   values at 20 °C match those obtained from the Nonius Kappa CCD room-temperature

193   measurement of the very same dwornikite single crystal.

194   All structure refinements were performed on F^2 with SHELXL-97 (Sheldrick 2008) in

195   the 'traditional' non-reduced kieserite cell setting. Scattering curves for neutral atoms were

196   used. The Mg/Ni ratios of the particular single crystals studied were extracted as a refined

197   variable in the respective structure refinement runs.

198   CIF data for room temperature structures included in Tables 2 and 3 (plus CIF of

199   endmember kieserite from Bechtold and Wildner 2016) and of temperature-dependent

200   structure investigations included in Tables 4 and 5 have been deposited with the submission at

201   the MSA website.

202

203   **IR spectroscopy**

204   The general procedure followed that for the comparable investigations on the kieserite-

205   szomolnokite solid solution by Talla and Wildner (2019). A part of each sample batch was

206   ground by hand in an agate mortar. For our purposes, the obtained sample powder with the

207   size of the largest crystallites not exceeding 100μm did not have to be sieved or treated in any

208   additional way, since grain size influences only band amplitudes but not their wavenumber

209   position (Jamieson et al. 2014), because only the latter parameter is dependent on chemical

210   composition. FTIR (Fourier Transform InfraRed) measurements were conducted in

211   transmission, ATR (Attenuated Total Reflectance) and DRIFT (Diffuse Reflectance Infrared

212   Fourier Transform) modes were done by means of the Bruker Tensor 27 FTIR spectrometer

213   (Globar light source, KBr beam splitter, DTGS detector). For transmission measurements, the

214   powdered sample material was diluted in KBr at a weight ratio of 1:300 and pressed into

215   pellets under a vacuum press. ATR measurements were done using the mountable Bruker

216   ATR unit by pressing the sample powder against the diamond surface. For DRIFT

217   measurements, the powder was pressed into the appropriate sample holder of a Perkin–Elmer

218   DRIFT unit. Finely ground MgO was used as the reflectivity standard for the background

219   measurements. All reflectance data were converted via the Kubelka-Munk equation

220   implemented in the Bruker OPUS software. The full wavenumber range (7000–400 cm^{-1}) was

221   investigated in all analytical modes. The instrumental spectral resolution was 4 cm^{-1}. Each

222   measurement was averaged from 50 individual scans to reduce noise. In the scope of the

223   DRIFT analyses, each sample was measured in pure state, as well as diluted with KBr in a

224   ratio of 1:20, to enhance the absorption contribution to the resulting spectrum.

225   Low-temperature FTIR transmission measurements were done on KBr micropellets (2

226   mm aperture diameter in a steel gasket, sample dilution ratio 1:300) using a Linkam FTIR600

227   cooling stage equipped with KBr windows. Measurements were done in 40 K intervals

228   ranging from 313 K (40 °C) down to 113 K (–160 °C). Some additional measurements at 93

229   K (–180 °C) were done occasionally.

230   Our usage of wavenumbers ν (in cm^{-1}) as the principal spectral unit in text and figures,

231   as opposed to wavelengths λ (in μm), is justified by its direct proportionality to the energy of

232   the incident photons. The corresponding wavelengths can be easily obtained via the formula

233    $\lambda(\mu m) = 10000/\nu(cm^{-1})$.

234

235   **Raman spectroscopy**

236   Raman spectra were measured on a Horiba Jobin Yvon LabRam–HR spectrometer,

237   equipped with an Olympus BX41 optical microscope. The diffraction grating with 1800

238   grooves/mm and the 633 nm laser were chosen. The system is equipped with an Si-based,

239   Peltier-cooled charge-coupled device (CCD) detector. A 100× objective (NA = 0.55) was

240   used for all room-temperature measurements. The wavenumber accuracy was better than 0.5

241   cm^{-1}, and the spectral resolution was determined to be ~0.3 cm^{-1}. Room-temperature Raman

242   spectra were acquired in tandem with DRIFT measurements (see above), taking advantage of

243   the powdered material for IR spectroscopy already being contained within a convenient

244   sample holder. All Raman spectra were acquired between 100–4000 cm^{-1} shift, using multi-

245   window scans with a counting time of 50 s per window and repeating every scan twice to

246   eliminate spikes.

247   Low-temperature Raman measurements were conducted on single crystals using the

248   Linkam FTIR 600 cooling stage. Despite varying and unknown crystal orientation, the use of

249   single crystals with significantly better scattering, allowing shorter measuring times (5 s per

250   window) was essential to mitigate ice buildup on the sample surface during cooling. The

251   crystals were placed on the Ag-block of the cooling stage covered with a thermal conducting

252   fluid. The bulky stage necessitated the use of a long-distance objective with a 50×

253   magnification (focal distance 10.6 mm), with the same setup of the Raman instrument

254   otherwise. The spectra were acquired in two separate spectral regions, from 100 to 1600 and

255   from 2800 to 4000 cm^{-1} shift. Most acquisition temperatures matched those used during FTIR

256   temperature-dependent investigations to allow for direct comparison.

257   Band positions for both FTIR and Raman spectra were obtained by fitting the spectra

258   with Voigt-shaped band profiles with the program Peakfit (Jandel Scientific, version 4.0).

259   Initial estimates of the number of bands and their distribution in IR and Raman spectra were

260   based on the investigations done on kieserite by previous authors (Stoilova and Lutz 1998;

261   Lane 2007; Lane et al. 2015 for FTIR spectroscopy; and Chio et al. 2007 and citations therein,

262   for Raman spectra). Linear regression analysis of FTIR and Raman data was accomplished

263   using the inbuilt statistical module of the program SigmaPlot 13.

264

265 **UV-Vis-NIR spectroscopy and crystal field calculations**

266   An unpolarized optical absorption spectrum of a single crystal of $NiSO_4 \cdot H_2O$ was

267 measured at room temperature in the spectral range 32000–5000 cm^{-1} on a mirror-optics

268 microscope IRscope-II, attached to a Bruker IFS66v/S FT-spectrometer, using a measuring

269 spot of 165 μm. A KBr beam splitter and appropriate combinations of light sources (Xe- or

270 W-lamp) and detectors (GaP-, Si-, Ge-diodes) were used to cover the spectral range. The final

271 spectrum is combined from three partial spectra (UV and Vis segments: 32000–10000 cm^{-1},

272 both at 40 cm^{-1} spectral resolution and averaged from 512 scans; NIR: 10000–5000 cm^{-1} at 20

273 cm^{-1} spectral resolution, 256 scans). The UV and NIR spectral segments were each aligned in

274 absorbance to match with the unadjusted Vis spectrum at 20000 and 10000 cm^{-1}, respectively,

275 and then converted to the linear absorption coefficient α.

276   Crystal field (CF) calculations were performed with the HCFLDN2 module of the

277 computer program package by Y.Y. Yeung (Chang et al. 1994), based both on classical CF

278 parameters assuming a pseudotetragonal field (according to the octahedral [4+2]

279 coordination) as well as in the framework of the semi-empirical Superposition Model (SM) of

280 crystal fields. In the latter case, the reference metal–ligand distance R_0 was set to 2.06 Å, the

281 mean <Ni–O> bond length in dwornikite, and some parameters were fixed to reduce the

282 number of variables (namely $t_2 = 3$, i.e., the 'electrostatic' value, and Racah C/B = 4.2, as

283 obtained in the classical approach). For further details concerning the calculation procedures

284 the reader is referred to comparable approaches in Wildner et al. (2013) and respective

285 references therein.

286

287   **Results**

288

289 **Sample chemistry and powder X-ray diffraction**

290   The wet chemical analyses yielded the actual Mg/Ni ratio in the synthesized bulk

291   products in their respective final state, i.e., after the purification process by water and ethanol,

292   described in the 'Experimental' section. They revealed systematic differences between the

293   pre-adjusted and the actual Mg/Ni ratio in the product. As is evident from Fig. 1, the synthesis

294   approach greatly influences the extent of discrepancy between pre-set and experimental x_{Ni}

295   values. Samples prepared by the evaporation technique show a convex trend with relative Ni

296   depletion peaking in intermediate members of the solid solution. The few finely crystalline

297   samples prepared in a fully sealed hydrothermal autoclave at 210 °C show pronounced Ni-

298   deficiency with the major part of Ni^{2+} remaining in solution. Details of the chemical

299   composition of samples used for FTIR and Raman spectroscopy are presented in Table 1. The

300   material obtained by the hydrothermal 'leaking vessel approach' yielded larger crystal

301   individuals. Because this material was intended for single-crystal measurements, the Mg/Ni

302   ratios of individual hand-picked crystals were extracted as a variable parameter in the

303   respective structure refinements.

304   Powder X-ray diffraction measurements and Rietveld refinements confirmed that the

305   batches consist nearly exclusively of kieserite-group $(Mg,Ni)SO_4 \cdot H_2O$ phases; occasional

306   traces of nickelhexahydrite were found. The diffraction patterns showed no signs of peak

307   splitting or abnormal broadening, thus confirming compositional homogeneity and the mono-

308   phase character of the obtained kieserite-group solid solutions.

309

310   **Crystal structures**

311   Crystal data and details of the data collections and structure refinements of four selected

312   representatives of the $Mg_{1-x}Ni_xSO_4 \cdot H_2O$ solid solution, including the dwornikite endmember,

313   are summarized in Table 2, respective final atomic coordinates and displacement parameters

314   are listed in Table 3. Corresponding temperature-dependent data of the dwornikite

315   endmember are compiled for three selected temperatures in Tables 4 and 5. Room-

316   temperature data for endmember kieserite used throughout the present paper are given in

317   Bechtold and Wildner (2016), temperature-dependent data of $MgSO_4 \cdot H_2O$ are found in Talla

318   and Wildner (2019).

319   The structural behavior of the kieserite-dwornikite solid solution series,

320    $Mg_{1-x}Ni_xSO_4 \cdot H_2O$, as derived from single-crystal X-ray diffraction measurements, is

321   illustrated in Figures 2–4, and relevant crystal chemical data of four selected representatives

322   including the dwornikite endmember are given in Table 6. Respective details for endmember

323   kieserite from Bechtold and Wildner (2016) are included for easy reference.

324   The kieserite structure type consists of kinked chains of O3($\equiv H_2O$)-corner-sharing

325    $MgO_4(H_2O)_2$ octahedra, clearly elongated along the octahedral water-water axis, with

326   adjacent octahedra being further intra-linked by nearly regular SO_4 tetrahedra via common O2

327   corners. These octahedral-tetrahedral chains are aligned parallel to the c –axis and interlinked

328   to a framework structure by sharing the polyhedral O1 corners as well as by moderately

329   strong hydrogen bonds O3···O2.

330   The present X-ray measurements and structure refinements do not indicate any

331   octahedral Mg-Ni cation ordering, domain formation or related effects. Figure 2 shows the

332   variation of the lattice parameters between kieserite and dwornikite. It is evident that

333   complete miscibility exists and that the solid solution series behaves according to Vegard's

334   law (Vegard 1921), with all lattice parameters changing in a linear way across the entire

335   composition. The cell volume V (–13.0 $Å^3$), angle β (–0.25°), and the lattice parameters a, b

336   and c (–0.08, –0.03 and –0.18 Å, respectively) all decrease with Ni uptake. This is mainly

337   driven by the clear decrease of the average metal-oxygen (Me–O) bond length and of the

338   octahedral volume upon Ni intake, as shown in Figs. 3a and 4a. The strongest reduction in

339   individual bond lengths occurs for the Me–O3 bonds with the major vector component

340   parallel to the c –axis, thus resulting in its strong decrease. The Me–O1 and Me–O2 bonds

341   change much less, Me–O1 even increases slightly (Figs. 3a, Table 6). Overall, the octahedral

342   shape is preserved as a clear [4+2] coordination in dwornikite. In contrast to the octahedron,

343   the tetrahedral SO_4 group slightly expands with increasing Ni-content, but tetrahedral bond

344   length and also angular changes (Fig. 3d) rarely exceed a 3σ limit. The donor–acceptor

345   distance of the medium-strength hydrogen bond O3–H···O2 shortens significantly at higher Ni

346   contents (Fig. 4c).

347   Further factors contributing to the shrinkage of the unit cell with increasing Ni-content

348   are polyhedral rotations and tiltings, evidenced by a significant decrease of the two Me–O–S

349   angles shown in Fig. 4b, whereas the chain angle Me–O3–Me marginally increases. As a

350   consequence, the rather rigid SO_4 tetrahedron rotates by 3.2° around its twofold axis (also

351   compare Fig. 5 in Talla and Wildner 2019).

352   As expected, when temperature is reduced, the cell volume as well as β, a and c

353   decrease, but the b axis lengthens for dwornikite (Fig. 5), as also found for kieserite (Talla and

354   Wildner 2019). Also the mean Me–O bond lengths (Fig. 6a) and octahedral volumes (Fig. 5c)

355   decrease, mainly by reducing the longest Me–O3 bond, and, thus, octahedral distortion is

356   reduced too. S–O bond lengths and the tetrahedral volume show an artificial increase upon

357   cooling (Fig. 6d, 5c) due to changes in thermal motion: a 'simple rigid bond' correction

358   according to Downs et al. (1992) reveals practically constant <S–O> bond lengths along the

359   full temperature range. The comparatively short O3–H···O2 hydrogen bond in dwornikite

360   further shortens, but by only about half the extent compared to kieserite (Talla and Wildner

361   2019). A roughly analogous situation is also found for the polyhedra-linking Me–O–S angles

362   in dwornikite which further decrease upon cooling, but less so than in kieserite (and

363   szomolnokite, Talla and Wildner 2019).

364

365   **IR spectra**

366   The IR spectra of $(Mg,Ni)SO_4 \cdot H_2O$ feature several clearly discernible absorption

367   features (Fig. 7). In the FTIR spectra measured in transmission mode, the H_2O absorption

368 region is dominated by a prominent band at 3182–3057 cm^{-1} (3.14–3.27 μm), representing the

369 symmetric stretching vibration $v_{1(H_2O)}$ of the H_2O molecule. A broad shoulder at higher

370 wavenumbers (3367–3262 cm^{-1} / 2.97–3.07 μm) represents $v_{3(H_2O)}$, the antisymmetric H_2O

371 stretching mode. The band positions of both H_2O stretching vibrations decrease significantly

372 in their wavenumber position upon Ni intake (Fig. 9a, Table 8), whereas the H_2O bending

373 vibration $v_{2(H_2O)}$ remains practically stable (1525–1522 cm^{-1} / 6.56–6.57 μm). The same

374 applies for the position of the strongest band in a major band group corresponding to the

375 antisymmetric $v_{3(SO_4)}$ stretching mode of the sulfate tetrahedra (a band group centered at

376 around 1150 cm^{-1} / 8.70 μm) and the IR-forbidden symmetric stretching mode $v_{1(SO_4)}$, visible

377 as a weak but well-defined band at around 1030 cm^{-1} (9.71 μm). A pronounced absorption

378 phenomenon, even considered as a potential diagnostic feature for kieserite-group compounds

379 by Lane et al. (2007, 2015), henceforth labeled 'Peak 900 cm^{-1}', occurs at wavenumbers from

380 884 to 941 cm^{-1} (11.31–10.63 μm) with increasing Ni content. Lastly, a band group at 630 cm^{-1}

381 (15.87 μm) is assigned to the tetrahedral $v_{4(SO_4)}$ bending modes.

382   It must be noted that the absorption band shape and even position vary between

383 individual FTIR measuring modes (Fig. 7, Table 8). As example, the symmetric stretching

384 vibration of the H_2O molecule occurs at 3182 cm^{-1} in kieserite measured in transmission

385 mode, whereas it is centered at 3165 cm^{-1} in ATR mode and as high as 3203 cm^{-1} using the

386 DRIFT technique on the very same sample. Nevertheless, the overall spectral appearance is

387 comparable, with the absorptions related to the H_2O bending vibration and the H_2O

388 combination modes being enhanced in DRIFT spectra (Fig. 7, Fig. 8, respectively), especially

389 on pure sample material. Contrary to this specific benefit of using undiluted material,

390 significant features such as the 'Reststrahlen band' (labeled 'R' in Fig. 7), a pronounced

391 absorption at around 1300 cm^{-1}, obscure the expected intrinsic sulfate vibrations between

392 1300 and 370 cm^{-1}. The spectral position of these features, however, is also dependent on the

393   sample composition, e.g., the Reststrahlenband decreases in position from 1360 to 1286 cm^{-1}

394   (7.35–7.77 µm) between kieserite and dwornikite.

395   The enhanced amplitude of absorption bands assigned to H_2O combination modes in the

396   4400–5200 cm^{-1} (2.27–1.92 µm) spectral region in diffuse reflectance spectra of undiluted

397   sample material allows for their meaningful evaluation. Three distinct bands occur in this

398   region at 4688, 4845 and 5087 cm^{-1} (2.13, 2.06 and 1.97 µm, respectively) in kieserite. As the

399   Ni content increases, both peripheral bands diverge from the original central band position for

400   kieserite at 4845 cm^{-1} to 4566 and 5110 cm^{-1} (2.19 and 1.96 µm, respectively), thus enhancing

401   the band separation with increasing Ni (Fig. 8ab), while the central band itself shifts down to

402   4735 cm^{-1} (2.11 µm).

403   In many cases, the observed changes in spectral band position are rather limited, such as

404   for the sulfate vibrations with ≤ 30 cm^{-1} in all three measuring modes, and that of the H_2O

405   bending mode, with a minimal decrease of only 3 cm^{-1} from kieserite to the dwornikite

406   endmember.

407   Pronounced linear correlation trends can be observed for the H_2O stretching vibrations,

408   where the well-resolved $\nu_{1(H_2O)}$ band changes in position from 3182 to 3057 cm^{-1} and the

409    $\nu_{3(H_2O)}$ shoulder decreases in wavenumber from 3367 to 3262 cm^{-1} between kieserite and

410   dwornikite. A somewhat smaller but still prominent linear change can be seen for the apparent

411   kieserite-group 'diagnostic' absorption band (Lane et al. 2007, 2015), increasing from 884 in

412   kieserite to 941 cm^{-1} with increasing Ni content (Fig. 9a).

413   The variation in the wavenumber position of the relevant spectral absorption

414   phenomena in the scope of the individual measurement modes, as well as the respective linear

415   regression coefficients are summarized in Table 8.

416   The results of FTIR measurements at low temperature, depicted for the Mg-Ni solid

417   solution series in Fig. 10a, show significant changes in the wavenumber position of the H_2O

418   stretching vibrations, which decrease significantly upon cooling. On the contrary, the

419 'diagnostic' band at ~900 cm^{-1} increases in wavenumber. The vibrations of the sulfate

420 tetrahedra remain nearly unaffected throughout the entire temperature range, as is also true for

421 the H_2O bending vibration. Reduced fitting accuracy obscures any observable temperature-

422 related trend for the $\nu_{3(H_2O)}$ band (Fig. 10a).

423

424 **Raman spectra**

425 The Raman spectra consist of numerous narrow bands in the 100–1600 cm^{-1} shift

426 region, with much better resolution compared to FTIR spectra (Fig. 9 vs. 11a). The most

427 prominent band is the symmetric stretching vibration $\nu_{1(SO_4)}$ of the sulfate tetrahedron at 1042

428 and 1020 cm^{-1} shift in kieserite and dwornikite, respectively. Several relevant spectral features

429 occur at lower shift values, the most prominent situated at ~220, ~430 and a doublet at ~630

430 cm^{-1} shift. Weak bands occur in the 1100–1600 cm^{-1} spectral region. With the exception of the

431 somewhat broader peak at roughly 1500 cm^{-1} (H_2O bending vibration), these bands are

432 assigned to the split $\nu_{3(SO_4)}$ vibration (Stoilova and Lutz 1998; Chio et al. 2007). Stretching

433 vibrations of the H_2O molecule are visible in the expected spectral region with the

434 antisymmetric $\nu_{3(H_2O)}$ contribution present as a mere poorly defined shoulder of the $\nu_{1(H_2O)}$

435 band, which decreases from 3179 down to 3071 cm^{-1} with increasing Ni-content (Fig. 12a,

436 Table 9). The position of the H_2O bending mode remains constant in analogy to FTIR results,

437 while most sulfate-related bands show a slight decrease upon Ni uptake with the exception of

438 the two peaks assigned to the $\nu_{2(SO_4)}$ bending mode in the ~400-500 cm^{-1} shift spectral region

439 (Fig. 12a). The position of the band at ~220 cm^{-1} shift assigned by Chio et al. (2007) to a

440 translational mode of H_2O and the MeO_6 octahedra increases significantly upon Ni uptake, as

441 is also observed for the band assigned to 'lattice modes' at ~120 cm^{-1} shift.

442 Linear changes in band position can also be seen in the Raman spectra acquired across

443 the $(Mg,Ni)SO_4 \cdot H_2O$ solid solution, as could be expected from the FTIR results (Table 9).

444 Fig. 12a illustrates the situation in detail, while Table 9 gives the respective coefficients of the

445 linear regression between the band position and x_{Ni}.

446 Raman measurements at low temperature show a significant temperature dependence of

447 the spectral position of certain modes, in analogy to the results of low-temperature FTIR

448 measurements. The very good resolution and low FWHM of the bands in Raman spectra

449 allow to accurately examine even the subtle positional changes of sulfate modes, which are

450 not so apparent in IR spectra (Table 9). In some cases, unfortunately, the amplitude of some

451 of the monitored Raman bands is largely suppressed due to an unfavorable respective crystal

452 orientation, causing increased errors upon fitting.

453 Despite this, a composition-independent systematic shift of the band position with

454 temperature is seen mainly for the $\nu_{1(H_2O)}$ band, which decreases in wavenumber by about 30

455 cm^{-1} across the full temperature range from +40 to –196 °C, and represents the strongest

456 observable change among all examined bands. As a shoulder of the well-defined $\nu_{1(H_2O)}$ band,

457 the $\nu_{3(H_2O)}$ band is generally poorly resolved, thus impeding any precise fit. The wavenumber

458 change with temperature for bands related to sulfate vibrations is, as seen also in FTIR

459 spectra, quite small, in general never exceeding 10 cm^{-1} in the examined temperature range

460 (Table 9). A systematic increase in wavenumber is observed at low temperature for the

461 lowest-energetic bands, representing Mg(Ni)–O stretching modes according to Chio et al.

462 (2007). For all observed bands, the rates at which the band positions change with temperature

463 remain constant across the entire examined temperature range, allowing to determine a mean

464 shift value per 1 °C for the individual bands, included in Table 9.

465

466 **UV-Vis-NIR spectroscopy and crystal field calculations**

467 The optical absorption spectrum of dwornikite is shown in Fig. 13. Three intense crystal

468 field absorption bands are observed around 8100, 13450 and 24600 cm^{-1}, which are assigned

469 to spin-allowed electronic transitions from the $^3A_{2g}(F)$ ground state to the $^3T_{2g}(F)$, $^3T_{1g}(F)$ and

470    $^3T_{1g}(P)$ levels of Ni^{2+} ($3d^8$ electron configuration) in octahedral (O_h) symmetry. The latter two

471   bands are modified by spin-forbidden states, i.e., $^1E_g(D)$ within the high-wavenumber slope of

472   the mid-energy band, and $^1T_{2g}(D)$ near the onset of the high-energy band; the structures below

473   6600 cm^{-1} originate from vibrational combination and overtone modes of the H_2O molecule.

474   Evidently, no significant splitting of the first and third spin-allowed bands is observed, either

475   by the naked eye or via peak-fitting analyses, as would be expected from the geometric [4+2]

476   elongation of the NiO_6 octahedron (Table 6, Fig. 3a). A splitting might be postulated for the

477   middle spin-allowed band (with the main component at 13450 cm^{-1}), but due to spin-orbit

478   mixing and intensity stealing by the spin-forbidden $^1E_g(D)$ level, the position and intensity

479   contribution of this second split component of $^3T_{1g}(F)$ can only be roughly estimated (~14800

480   cm^{-1}). The refined crystal field and interelectronic repulsion parameters resulting from these

481   assignments are summarized in Table 10, and respective observed and calculated energy

482   levels (from the 'classical' tetragonal CF approach) are included in Fig. 13.

483

484   **Discussion**

485

486   **Crystal structural evolution and crystal chemistry**

487   The present crystal structure investigations corroborate the existence of a continuous

488   solid solution series, $Mg_{1-x}Ni_xSO_4·H_2O$, between kieserite, $MgSO_4·H_2O$, and isotypic

489   dwornikite, $NiSO_4·H_2O$. In view of previous crystal structure investigations of the two

490   endmembers (for kieserite: Bechtold and Wildner 2016; Hawthorne et al. 1987; for

491   dwornikite: Wildner and Giester 1991), the respective solid solution series behaves according

492   to 'basic' expectations. In particular, all lattice parameters and crystal chemical data exhibit

493   Vegard-type behavior within the limits of error, undergoing linear changes with progressing

494   Mg/Ni ratio. This trend serves as basis for any further theoretical calculations of interest, and

495   the significant linear changes between the endmembers importantly allow, amongst others, to

496 infer the Mg/Ni ratio in binary kieserite-group samples of unknown composition from X-ray

497 data. Vegard-type behavior indicates one-site ideal mixing of the endmembers (Powell and

498 Holland 1993), as is also the case with the recently investigated kieserite-szomolnokite solid

499 solution (Talla and Wildner 2019). Enthalpy, entropy, molar volume, as well as heat capacity

500 and thermal expansion can be determined by the linear combination of these parameters for

501 both endmembers in their respective formula ratio in the sample (van Hinsberg et al. 2005a,b).

502   Likewise, the crystal chemical expectations are fulfilled in the sense that the

503 replacement of the larger Mg cation (r_{Mg} = 0.720 Å) by the smaller Ni^{2+} (r_{Ni2+} = 0.690 Å; all

504 radii from Shannon 1976) leads to a decrease of the Me–O2 and especially Me–O3 bond

505 lengths as well as of the average <Me–O> distance, and consequently to a reduction of the

506 respective octahedral and the unit-cell volume (Figs. 2b, 3a and 4a). Due to a slight increase

507 of the Me–O1 bonds with Ni-content, a characteristic [4+2] coordination of the MeO_6

508 polyhedron is also realized in dwornikite (as in kieserite and most other kieserite-group

509 sulfates, e.g. cobaltkieserite, Bechtold and Wildner 2016) rather than tending towards a

510 [2+2+2]-type coordination, such as for the FeO_6 polyhedron in szomolnokite (Talla and

511 Wildner 2019). In the latter case of the Mg-Fe solid solution (r_{Fe2+} = 0.780 Å), the cell

512 parameters (except for the *b*-axis) and all Me–O bond lengths significantly increase with Fe

513 content.

514   In contrast to the octahedron, the tetrahedral SO_4 group very slightly expands with

515 increasing Ni-content (Figs. 3c, 4a), a behavior analogously observed in the respective Mg-Fe

516 and Mg-Co solid solutions (Talla and Wildner 2019; Bechtold and Wildner 2016). The

517 donor–acceptor distance of the medium-strength hydrogen bond O3–H···O2 shortens

518 significantly at higher Ni contents (Fig. 4c), with important impact on the vibrational spectra

519 discussed below.

520   The unit-cell contraction is not only driven by reduction of the Ni–O compared to the

521 Mg–O bond lengths (Fig. 3a), but further intensified by octahedral-tetrahedral tiltings via

522   reduced Me–O–S angles with increasing x_{Ni} (Fig. 4b), meaning that the contraction exceeds

523   the one expected from the mere differences in the Me^{2+} ionic radii. This finding parallels

524   those observed for the kieserite-cobaltkieserite (Bechtold and Wildner 2016) and kieserite-

525   szomolnokite (Talla and Wildner 2019) solid solutions, and has been attributed by these

526   authors to the absence (for Mg), respectively the presence (for Co, Fe; here: Ni), of $3d$-

527   orbitals; hence, for detailed discussions on this subject, which fully applies to the present case

528   of the replacement of Mg by Ni, the reader is referred to those papers (and references therein).

529   Similarly, the apparent difference in the character of the octahedral bond length distortion,

530   i.e., a clear [4+2]-type elongation in kieserite, dwornikite and all other kieserite-group

531   endmember compounds except szomolnokite, which displays a tendency towards a [2+2+2]

532   distortion, has been amply addressed by Talla and Wildner (2019), linking it with the $3d$-

533   electron configuration of the particular Me^{2+} cation.

534

535   **IR, Raman and crystal field spectra**

536   **IR spectra at ambient conditions.** The linear Vegard-type behavior observed in the

537   structural data for the $Mg_{1-x}Ni_xSO_4 \cdot H_2O$ solid solution series (Figs. 2–4) is also reflected in

538   the results of FTIR and Raman spectroscopic measurements. With wavenumber units in use,

539   linear shifts of the IR spectral bands positions across the kieserite-dwornikite solid solution

540   series (Fig. 9a, Table 8) are recognized, in principle allowing to deduce the respective Mg/Ni

541   ratio solely from spectroscopic data.

542   The evidence that the wavenumbers of both stretching modes of the H_2O molecule,

543     $\nu_{1(H_2O)}$ and $\nu_{3(H_2O)}$, decrease upon Ni uptake is in agreement with the single-crystal X-ray

544   results (Fig 4c, Table 6), where a decrease in the hydrogen bond length between the O3 donor

545   and the O2 acceptor oxygen with increasing x_{Ni} can be correlated with the observed band

546   behavior according to well-established trends (Libowitzky 1999). The opposite behavior

547   occurs in the kieserite-szomolnokite solid solution, where Fe contents lead to the lengthening

548   of the O3···O2 donor-acceptor distance, resulting in an increase in wavenumber observable

549   mainly for the $\nu_{1(H_2O)}$ stretching mode (Talla and Wildner 2019, Fig. 9b). The more or less

550   constant position of the bending vibration of the H_2O molecule independent of the Ni content

551   indicates a rigid character of the H_2O molecule, despite the widening of the acceptor–donor–

552   acceptor angle O2–O3–O2 from kieserite to dwornikite (136.7–140.5°). Both the symmetric

553     $\nu_{1(SO_4)}$ vibration and the three bands assigned to the split $\nu_{3(SO_4)}$ mode (Chio et al. 2007)

554   slightly decrease in wavenumber position with increasing x_{Ni}, in accord with the observed

555   slight relaxation of the SO_4^{2-} tetrahedron reflected in the elongation of S–O bond lengths

556   towards dwornikite (Figs. 3c, 4a, Table 6). Of the three bands assigned to the $\nu_{3(SO_4)}$ vibration,

557   only the major one is depicted and its position followed in Fig. 9a and Table 8. In contrast to

558   the diverging trends found for the hydrogen bonding schemes and O–H stretching vibrations,

559   the structural and spectroscopic sulfate behavior upon Ni uptake is closely comparable with

560   the situation recently investigated (Talla and Wildner 2019) for Fe uptake in the kieserite–

561   szomolnokite series (Fig. 9a,b). The prominent absorption band at ~900 cm^{-1} deemed as

562   'diagnostic' by Lane et al. (2015) shows a rather pronounced wavenumber increase towards

563   Ni-rich compositions, as opposed to its behavior upon Fe uptake (Fig. 9a,b). This band is

564   usually assigned to a librational mode of the H_2O molecule (e.g. Lane 2007; Lane et al. 2015),

565   which is supported by its contradicting behavior in case of the Mg-Fe and Mg-Ni solid

566   solutions, such as in the case of the H_2O stretching modes. Alternatively, considering the low-

567   temperature behavior described below, the band may be also attributed to a combination mode

568   of the sulfate and octahedral vibration modes (Talla and Wildner 2019). A group of bands at

569   ~630 cm^{-1} (Fig. 7), assigned by Lane et al. (2015) to the $\nu_{4(SO_4)}$ vibration, can hardly be

570   exploited for cosmochemical considerations, as the spectral region not only consists of

571   numerous peaks with varying FWHM, but also is not clearly discernible from the signals of

572   other sulfates (Cloutis et al. 2006) and also of atmospheric CO_2. Therefore, the IR spectral

573   region between 700 and 300 cm^{-1} (14.3–27.0 μm) was not studied in further detail.

574   Contrary, the 4400–5200 cm^{-1} (2.27–1.92 μm) spectral region, where combination

575   modes of the H_2O stretching and bending vibrations induce absorptions, is considered by

576   many authors to be an important spectral signature in reflectance spectra, allowing not only to

577   discern kieserite from other sulfate hydrates, in which these bands occur at higher

578   wavenumbers (Mangold et al. 2008; Noel et al. 2015), but also to roughly infer either its Fe

579   content (Cloutis et al. 2006; Bishop et al. 2009; Liu et al. 2016, Talla and Wildner 2019) or Ni

580   content (this work), due to the opposite behavior of the respective group of bands in the two

581   binary sulfate monohydrate solid solutions. The H_2O combination modes are most apparent in

582   diffuse reflectance spectra measured on undiluted sample material, whereas they are largely

583   suppressed and too faint to be tracked effectively in the other measuring modes. The kieserite

584   endmember shows a typical set of three bands at 4688, 4845 and 5087 cm^{-1} (2.13, 2.06, 1.96

585   μm) (Fig. 8ab, Table 8). The two lower-energetic components decrease significantly to 4566

586   and 4735 cm^{-1} (2.19 and 2.11 μm), respectively, in the dwornikite endmember, whereas the

587   peak at the highest wavenumber increases to 5110 cm^{-1} (Fig. 8a). In case of Fe-rich solid

588   solutions and pure szomolnokite, the peripheral bands show opposite behavior, converging to

589   the central one while largely maintaining the overall spectral position of the triplet. The

590   highest-energetic band is always rather weak, even creating the misleading impression of a

591   single broad absorption in the case of szomolnokite, since it occurs but as a weak shoulder in

592   the bandgroup (Talla and Wildner 2019).

593   The afore-mentioned impact of the sample dilution on DRIFT spectra and their artifacts

594   has important implications for orbiter measurements, where IR spectra reflected by 'fluffy'

595   kieserite aggregates (more transmission) would somewhat differ in shape and band position

596   from signals acquired on compact kieserite masses or crusts due to the different

597   reflection/transmission ratio of the particular material. Disregard of these issues could

598   complicate the assessment of the properties and composition of the measured monohydrate

599   sulfate. Contrary, the grain size seems to have little effect on band *position* in IR reflectance

600   spectra (Jamieson et al. 2014; Pitman et al. 2014).

601   According to their divergent behavior in the IR spectra, the H_2O-related bands allow to

602   easily discern between Fe or Ni enrichment in the ideal case of a purely binary

603    $Mg_{1-x}Me_xSO_4 \cdot H_2O$ solid solution at ambient temperature (Table 8). In case of Ni contents, the

604   wavenumbers of the H_2O stretching modes $\nu_{1(H_2O)}$ and $\nu_{3(H_2O)}$ are always lower than in

605   endmember kieserite. Conversely, respective Fe enrichment is indicated by a higher

606   wavenumber mainly of the $\nu_{1(H_2O)}$ stretching vibration compared to pure kieserite (Talla and

607   Wildner 2019, Fig. 9a,b). In addition, the H_2O combination mode region centered at ~4900

608   cm^{-1} (2.04 μm) in DRIFT spectra is a further promising candidate for the assessment of Ni or

609   Fe contents, due to the opposite behavior of the peripheral bands (Fig. 8, Table 8). Likewise,

610   the band at ~900 cm^{-1} (11.1 μm) is another candidate allowing to discern between Fe or Ni

611   contents, since it increases in wavenumber by 57 cm^{-1} in case of Ni uptake towards the

612   dwornikite endmember, but decreases by roughly 50 cm^{-1} in szomolnokite in respect to the

613   kieserite endmember benchmark. The H_2O bending vibration as well as the sulfate modes all

614   show but minor changes in respect to the sample chemistry. These are comparable

615   irrespective of the transition element substituting Mg (Fig. 9 a,b).

616

617   **Temperature dependence of IR spectra.** The discussion so far was limited to room-

618   temperature data. However, temperature-related changes are to be expected, not only for data

619   from Mars (+20 to −120 °C at latitudes < 40°; Witzke et al. 1997), but especially considering

620   the situation on the icy moons of Jupiter and Saturn with mean equatorial surface temperature

621   in the range of 90–100 K (e.g., on Europa, Ashkenazy 2019). The structural changes upon

622   temperature decrease are rather similar for dwornikite (Tables 4 and 7), kieserite and

623   szomolnokite (Talla and Wildner 2019), without any indication of a phase transition in either

624   case. Examining and comparing the respective acquired low-temperature IR-spectra (Fig.

625   10a,b), two aspects are evident. Firstly, all vibrations related to the sulfate group are more or

626   less stable in their wavenumber position regardless of temperature across either solid solution,

627   confirming their rigid character, regardless of the element substituting Mg. The H_2O-related

628   symmetric stretching vibration shows a comparable decrease in wavenumber position for the

629   Mg-Ni and Mg-Fe solid solutions (Talla and Wildner 2019), irrespective of composition. The

630   band at ~900 cm^{-1} in the Mg-Ni solid solution and at ~850 cm^{-1} in the Mg-Fe series (Fig.

631   10a,b) shows a wavenumber increase by about 0.07 cm^{-1}/°C across the +40 °C to −180 °C

632   temperature range in both solid solutions. The parallel reaction to temperature decrease, along

633   with the inverted correlation trends upon Ni- or Fe- incorporation in accord with the behavior

634   of the H_2O stretching modes, strongly hint this band to be linked to an H_2O-related

635   (librational) mode.

636   Surprisingly, the H_2O bending vibration remains nearly unaffected upon cooling (Fig.

637   10a,b), indicating no major influence of temperature on the internal molecular structure of the

638   water molecule, thus corroborating its 'rigid' character. Accordingly, the acceptor-donor-

639   acceptor angle O2–O3–O2 is rather insensitive to temperature (−1.0° change along 200 K),

640   compared to the significant influence of the Mg/Ni ratio (−3° change).

641

642   **Raman spectra at ambient conditions.** Raman spectra acquired across the Mg-Ni

643   solid solution series also show systematic band shifts with increasing x_{Ni} (Figs. 11a and 12,

644   Table 9). The linear trends and wavenumber shifts of related vibrational phenomena observed

645   in Raman spectra basically correspond to their behavior in FTIR spectra.

646   As expected, the decrease in hydrogen bond length with increasing Ni content reported

647   above, leads to the decrease in the wavenumber of the H_2O symmetric stretching vibration

648   from 3178 to 3071 cm^{-1} shift and that of the antisymmetric mode from 3388 to 3257 cm^{-1}. The

649   very good match between the wavenumber position observed in the IR transmission spectra

650   (Table 8) and Raman data (Table 9) underline the consistency of both sets of data. The

651   decrease in shift of the antisymmetric $\nu_{3(H_2O)}$ vibration is well visible in case of the Mg-Ni

652   solid solution (Fig. 12a), in analogy to the FTIR spectra (Fig. 10a), despite its position as a

653   weak shoulder of the dominant $\nu_{1(H_2O)}$ vibration. This is in sharp contrast to the kieserite-

654   szomolnokite solid solution (Fig. 12b), where no observable trend could be identified for the

655     $\nu_{3(H_2O)}$ mode (Talla and Wildner 2019). This contrast can be attributed to the much stronger

656   change of the hydrogen bond length between the kieserite and dwornikite endmembers (–

657   0.068 Å) (Fig. 4c) compared to the respective difference between kieserite and szomolnokite

658   (+0.012 Å; Talla and Wildner 2019).

659   The nearly perfect match between the behavior of the sulfate group in the Mg-Ni and

660   Mg-Fe kieserite solid solution, including the absolute positions of the corresponding sulfate-

661   related bands (Fig. 12), is remarkable. This is in agreement with the relaxation of the sulfate

662   tetrahedron (Fig. 3cd, Table 6) both in case of Fe and Ni incorporation (Talla and Wildner

663   2019). On the other hand, the assignment of the band at 500 cm^{-1} to sulfate-related modes by

664   Chio et al. (2007) is disputable, since this band shows opposite behavior in both solid

665   solutions (Fig. 12).

666   The bands observed in the 100–250 cm^{-1} spectral region feature a component at ~220

667   cm^{-1} assigned by Chio et al. (2007) to a vibration involving the translation along the Fe–H_2O

668   bond in szomolnokite. However, its spectral position remains nearly unchanged regardless of

669   the Mg/Fe ratio (Fig. 12b). A much stronger variation (an increase in wavenumber) is found

670   for the corresponding band in case of Ni uptake (Fig. 12a, Table 9). Presuming the

671   involvement of the H_2O molecule in the given Raman mode, more pronounced changes are

672   indeed to be expected in case of the Mg-Ni solid solution, since, as was already mentioned,

673   the hydrogen bonding system undergoes much stronger changes. (Fig. 9a,b, Fig. 12a,b, Tables

674   8 and 9 and Fig. 4c, Table 6). For the lowest mode at ~130 cm^{-1} a contradicting behavior in

675   case of Ni and Fe incorporation is observed. While we are unable to ascertain the exact

676   character of this vibrational mode, this difference suggests the involvement of octahedral

677   modes, since these polyhedra also show opposite structural trends between the Mg-Ni solid

678   solution (decrease in polyhedral volume and Me–O2,O3 bond lengths) and the Mg-Fe series

679   (increase of polyhedral volume and all Me–O bonds).

680

681   **Raman spectra at low-temperature conditions.** Band shifts in low-temperature

682   Raman spectra show similar behavior to corresponding vibrational modes in the IR spectra

683   (Table 9), and comparison with previous data for the Mg-Fe solid solution (Talla and Wildner

684   2019) reveal that they are largely independent of the cation substituting for Mg. As expected,

685   the $\nu_{1(H_2O)}$ vibration shows significant changes towards lower shift values upon cooling, while

686   the sulfate-related bands are rather stable. Better band resolution compared to IR spectra

687   allows to track even the subtle positional changes of these peaks. The highest-energy peak at

688   ~1200 cm^{-1} of the split $\nu_{3(SO_4)}$ vibration takes higher shift values, while a decrease in position

689   for the lowest-situated $\nu_{3(SO_4)}$ peak at ~1100 cm^{-1} shift can be observed (Table 9). The

690   symmetric stretching vibration $\nu_{1(SO_4)}$ shows a very minor decrease in wavenumber (Table 9).

691   The octahedra-related mode at ~220 cm^{-1} exhibits a notable increase in wavenumber at low

692   temperature, as does the lattice band at ~130 cm^{-1}. The complex nature of this low-energy

693   lattice mode does not allow reliable band assignment without ab-initio calculations, beyond

694   the scope and aim of the present study.

695

696   **Use of vibrational spectra to estimate Ni- and Fe-contents of (extraterrestrial)**

697   **kieserite.** Linear trends, observed for changes in structural parameters across the kieserite-

698   dwornikite solid solution (Figs. 2-4), as well as in the position of IR spectral bands (when

699   expressed in wavenumber units) and Raman spectra, clearly correlate with the Mg/Ni ratio

700   (Figs. 9, 11). Aside from documenting in detail the behavior of kieserite-group compounds

701   throughout the Mg-Ni solid solution series relevant to the icy moons of Jupiter and Saturn, the

702   linearity of the data also allows its straightforward use as a standard of comparison in

703   evaluating IR-spectra acquired by orbiters, as well as Raman measurements which could be

704   conducted during eventual rover missions. In this regard, the use of wavelength units (in μm)

705   to express spectral band positions, as it is common in the cosmochemical community, would

706   seem to be more appropriate. However, our preference for – and the benefits of – the use of

707   wavenumber units (cm^{-1}) throughout this work for discussion and depiction of spectroscopic

708   data have been amply discussed in our previous paper (Talla and Wildner 2019).

709   In general, the evaluation of orbiter measurements in the VNIR-MIR spectral range

710   (visible to near/medium infrared) leading to the assessment of the mineral phases present on

711   the surface of celestial bodies and their composition, follows the 'spectral unmixing'

712   approach, requiring reference endmember spectra, as is the case in the currently conducted

713   investigations of surface spectra from Mars (Cloutis et al. 2006; Combe et al. 2008; Mangold

714   et al. 2008; Bishop et al. 2009; Lichtenberg et al. 2010; Roach et al. 2010; Noel et al. 2015;

715   Liu et al. 2016). In brief, spectra from orbiter measurements are fitted by the least-squares

716   technique using reference endmember spectra to fit the measured signal after its correction for

717   the instrumental function (CRISM smile, etc.), atmospheric scattering (if relevant) and the

718   incidence angle using detailed knowledge of the local topography. While to this date, only

719   pure endmember kieserite spectra were used for this assessment, the discovery of linear trends

720   across the kieserite-dwornikite solid solution presented in this work as well as across the

721   kieserite-szomolnokite solid solution (Talla and Wildner 2019) allows to derive reference

722   spectra for monohydrate sulfates of an intermediate composition and, in principle, to obtain

723   additional information on the chemistry (Mg/Ni ratio in the present case) of the kieserite-

724   group sulfate monohydrate at hand, with semi-quantitative results at least. Two prominent

725   features in the IR spectra, which show a pronounced slope in their correlation with increasing

726   Ni content, are the symmetric and antisymmetric stretching vibration $v_{1(H_2O)}$ and $v_{3(H_2O)}$ of

727   H_2O, with a negative correlation to x_{Ni}, and the 'diagnostic' band at ~900 cm^{-1}, the

728   wavenumber of which increases with Ni content in contrast to the situation in the Mg-Fe solid

729   solution (Figs. 9, 12b, Table 8). The fact that the antisymmetric stretching mode $v_{3(H_2O)}$ of the

730   H_2O molecule shows a clear dependence on the Ni content can be regarded as an important

731   benchmark, allowing one to discern between Ni- and Fe-incorporation, since no such trend is

732   observed in case of Fe contents along the Mg-Fe solid solution (Talla and Wildner, 2019).

733   However, the two other promising features to infer the Ni content in the medium-infrared

734   region – $v_{1(H_2O)}$ and the diagnostic band at ~900 cm^{-1}, which show opposite behavior

735   compared to the Mg-Fe solid solution – are also the ones which show the strongest change in

736   wavenumber with decreasing temperature (Fig. 10). The same, considering the temperature

737   sensitivity of the fundamental H_2O bands, will apply to their combination modes in the ~4900

738   cm^{-1} region (Fig. 8ab), which, according to the results for kieserite of Jamieson et al. (2014),

739   split further apart with decreasing temperature. This behavior enhances the splitting of those

740   bands in addition to the effect of Ni incorporation, leading to a potential overestimation of x_{Ni}.

741   Despite being the exact opposite to the merging of these bands into a seemingly single broad

742   absorption with a shoulder upon Fe intake (Talla and Wildner 2019), the influence of

743   temperature complicates a reliable assessment of Ni contents in the examined material.

744   Anyway, the knowledge of surface temperatures (at least approximate values) during

745   remote measurements is a prerequisite to allow for meaningful quantitative comparisons,

746   otherwise only semi-quantitative information may be extracted. The rough estimation of

747   temperature is in part possible even from remote sensing spectra in themselves, because they

748   contain spectral regions which slightly shift according to the surface temperature, such as the

749   ~5000 cm^{-1} (2 μm) wavenumber region (Liu et al. 2016). Mid-infrared hyperspectral remote

750   sensing instruments (and bolometers) can provide radiance data. Because these follow Planck

751   behavior, they can easily be converted to emissivity by the application of a Planck function at

752   a given temperature, to provide accurate surface temperature values (for references see e.g.,

753   Ruff et al. 1997). In addition, any rovers, whether in the scope of present (Mars) or future

754   (e.g., the Jovian moons) missions, are typically equipped with thermometers, providing an

755 additional rough temperature value. The attempt to use sulfate-related bands for such

756 considerations is hampered by their wavenumber position being largely insensitive to

757 temperature changes in the IR spectra regardless of the substituting cation (Fe versus Ni), as

758 can be seen in (Fig. 10 a,b). This will likely prevent any exact observation of the subtle band

759 position changes also due to enhanced noise.

760   Additional sources of error arise from the use of different correction datasets preceding

761 the actual spectral unmixing procedure. Different versions of the atmospheric correction

762 model used in the evaluation of CRISM spectra from Mars may lead to significant changes in

763 the form of the resulting spectrum, even causing errors in the discrimination between kieserite

764 and szomolnokite in the same region of interest (Bishop et al. 2009, Noel et al. 2015).

765   A much more promising situation is to be expected considering the high resolution and

766 low FWHM of Raman bands, which aids in ascertaining their position changes from kieserite

767 to dwornikite with much higher precision when the Raman spectrometer is close to the target

768 (i.e, not from an orbital platform). While the superior spectral resolution allows efficient use

769 of the sulfate-related bands, such as the prominent $\nu_{1(SO_4)}$ band (Fig. 11), it is possible to

770 derive the *total* Mg/Me^{2+} (Me^{2+} = Fe^{2+} + Ni^{2+}) content only, because the sulfate modes behave

771 analogically in the case of Ni or Fe uptake, as opposed to the H_2O stretching vibrational

772 modes, that show opposite trends between Ni and Fe incorporation (Fig. 12a,b respectively).

773 These water bands are, however, weaker in the Raman spectra (Fig. 11) and are temperature-

774 sensitive.

775   Further complications arise if a ternary Mg/Fe/Ni solid solution is present. As described

776 above, the major difference in vibrational spectra of the Mg-Fe (Talla and Wildner 2019) and

777 Mg-Ni solid solution (this work) concerns the vibrational modes involving the H_2O molecule

778 (Fig. 9a,b). Structurally induced opposite trends are observed for both H_2O stretching modes.

779 In case of Fe uptake, mainly the symmetric $\nu_{1(H_2O)}$ mode undergoes changes, shifting to higher

780 wavenumbers as the O3···O2 donor–acceptor distance increases. This shift would be

781   dampened by the presence of Ni in a ternary solid solution. Fortunately, the antisymmetric

782    $v_{3(H_2O)}$ mode remains constant in position regardless of the Mg/Fe ratio (at ~3380 cm^{-1} in

783   FTIR transmission mode), whereas a prominent decrease of its position occurs in case of Ni-

784   incorporation, as shown in Fig. 9a,b. This opens up the chance to discriminate between Ni and

785   Fe contents in kieserite: taking the position of the antisymmetric H_2O stretching mode $v_{3(H_2O)}$

786   as reference to derive the Ni content, the Fe content may as well be estimated, based on the

787   difference between the position of the symmetric $v_{1(H_2O)}$ stretching mode expected from the

788   deduced Ni formula content, and its actual position, expectably at somewhat higher

789   wavenumbers (indicative of Fe content).

790   The total content of both transition elements (Ni and Fe) can in theory be verified via

791   the sulfate-related bands in Raman spectra if these are available (preferably using the

792   strongest $v_{1(SO_4)}$ band), because their positions are rather insensitive to temperature (see above

793   and Talla and Wildner 2019). They undergo the same changes to lower shift values,

794   irrespective of the transition element present.

795

796   **Crystal field spectra.** The crystal field (CF) spectrum of dwornikite (Fig. 13) shows

797   that VNIR spectra from orbiter or rover measurements might be influenced by Ni contents of

798   monohydrate sulfates, in particular by the broad first spin-allowed $^3A_{2g}(F)\rightarrow^3T_{2g}(F)$ band, at

799   ambient conditions centered at ~8100 cm^{-1} (~1.24 μm), but extending from 6400 to 10400

800   cm^{-1} (1.57 to 0.95 μm). Besides, a Superposition Model (SM) calculation applying the

801   ambient SM parameters from Table 10 to the octahedral NiO$_6$ geometry at −160 °C (Table 7)

802   reveals that temperature-dependent band shifts are expected to be negligible, i.e., 10 cm^{-1} for

803    $^3T_{2g}(F)$ to at most 20 cm^{-1} for the two higher-energetic $^3T_{1g}$ bands.

804   In agreement with the absence of any perceivable band splitting, at least for the first and

805   third spin-allowed band (Fig. 13), the obtained CF and SM parameters do not properly

806   reproduce the structural [4+2] elongation of the NiO$_6$ octahedron. In fact, with Dt = −10 cm^{-1}

807 even a faint polyhedral compression of the pseudotetragonal axis is indicated. This

808 discrepancy can be best explained by the higher CF strength of H_2O ligands forming the

809 elongated axis (compared to the oxygen ligands of the sulfate groups), in this way obviously

810 fully compensating the structural elongation. A similar but less pronounced partial

811 compensation effect was also found in the CF spectra of cobaltkieserite (Wildner 1996) and

812 szomolnokite (Talla and Wildner 2019). The same reasoning may also be applicable to some

813 of the extracted SM parameters, namely t_4 and $\overline{B}_2$, which yielded quite unrealistic low values.

814 Albeit, a tendency towards t_4 values much lower than their electrostatic ideal value ($t_4 = 5$)

815 has been observed previously for divalent transition metal compounds, among them also

816 cobaltkieserite (Andrut et al. 2004).

817

818 **Implications**

819

820 The presented data for the kieserite-dwornikite solid solution can assist cosmochemical

821 investigations, given the presence of kieserite-group sulfates on the surface of Mars and

822 potentially on the Jovian moons, where conditions are favorable for their formation. The

823 linear character of the observed spectral and structural trends at room temperature and the

824 knowledge of their changes upon cooling provides a solid starting basis to draw conclusions

825 about the content of Ni in kieserite based on absorption band positions in IR and Raman

826 spectra. Even in the unfavorable case of a semi-quantitative approach (no knowledge of

827 temperature), zoning of Ni contents in kieserite-containing sediments can be monitored using

828 the presented data. Given the change in the spectral position of the antisymmetric H_2O

829 vibration occurring only upon Ni-incorporation, a good chance to reliably estimate Ni versus

830 Fe contents in a ternary Mg-Fe-Ni-kieserite solid solution presents itself as well, presuming at

831 least a rough knowledge of the surface temperature on the investigated planetary body.

832

833 **Acknowledgments**

834

835   This work was supported by a grant from the Austrian Science Fund (FWF): P 29149-

836 N29. We thank R. Miletich, M. Ende, and J. Meusburger (all Vienna) for helpful discussions.

837 Assistance by G. Giester (Vienna) with the low-temperature X-ray data collections is

838 gratefully acknowledged. Author MW is grateful to Y.Y. Yeung (Hong Kong) for providing a

839 modified copy of his HCFLDN2 program. We thank the reviewers Henrik Skogby and

840 Melissa Lane for their constructive approach, which improved the quality of this paper in

841 many ways.

842

843 **References**

844

845 Anders, E. and Grevese, N. (1989) Abundances of the elements: Meteoritic and solar. Geochimica et

846   Cosmochimica Acta, 53, 197–214.

847 Andrut, M., Wildner, M., and Rudowicz. C.Z. (2004) Optical absorption spectroscopy in geosciences.

848   Part II: Quantitative aspects of crystal fields. In A. Beran, E. Libowitzky, Eds., Spectroscopic

849   Methods in Mineralogy, p. 145–188. EMU Notes in Mineralogy 6, Eötvös Univ Press, Budapest.

850 Ashkenazy, Y. (2019) The surface temperature of Europa. Heliyon, 5, e01908, 1–11.

851 Bechtold, A., and Wildner, M. (2016) Crystal chemistry of the kieserite–cobaltkieserite solid solution,

852      $Mg_{1-x}Co_x(SO_4) \cdot H_2O$: well behaved oddities. European Journal of Mineralogy, 28, 43–52.

853 Bishop, J.L., Parente, M., Weitz, C.M., Noe Dobrea, E.Z., Roach, L.H., Murchie, S.L., McGuire, P.C.,

854   McKeown, N.K., Rossi, C.M., Brown, A.J., Calvin, W.M., Milliken, R., and Mustard J.F. (2009)

855   Mineralogy of Juventae Chasma: Sulfates in the light-toned mounds, mafic minerals in the

856   bedrock, and hydrated silica and hydroxylated ferric sulfate on the plateau. Journal of Geophysical

857   Research, 114, E00D09.

858 Brese, N.E., and O'Keeffe, M. (1991) Bond-valence parameters for solids. Acta Crystallographica,

859   B47, 192–197.

860 Brown, I.D., and Shannon, R.D. (1973) Empirical bond–strength–bond–length curves for oxides. Acta

861   Crystallographica, A29, 266–282.

862   Burgess, R., Wright, I.P., and Pillinger, P.T. (1991) Determinations of sulphur-bearing components in

863   C1 and C2 carbonaceous chondrites by stepped combustion. Meteoritics, 26, 55–64.

864   Chang, Y.M., Rudowicz, C., and Yeung, Y.Y. (1994) Crystal field analysis of the $3d^N$ ions at low

865   symmetry sites including the "imaginary" terms. Computers in Physics, 8, 583–588.

866   Chio, C.H., Sharma, S.K., and Muenow, D.W. (2007) The hydrates and deuterates of ferrous sulfate

867   ($FeSO_4$): a Raman spectroscopic study. Journal of Raman Spectroscopy, 38, 87–99.

868   Cloutis, E.A., Craig, M.A., Mustard, J.F., Kruzelecky, R.V., Jamroz, W.R., Scott, A., Bish, D.L.,

869   Poulet, F., Bibring, J.-P., and King, P.L. (2007) Stability of hydrated minerals on Mars.

870   Geophysical Research Letters, 34, L20202.

871   Combe, J.-Ph., Le Mouélic, S., Sotin, C., Gendrin, A., Mustard, J.F., Le Deit, L., Launeau, P., Bibring,

872   J.-P., Gondet, B., Langevin, Y., and Pinet, P. (2008) Analysis of OMEGA/Mars Express

873   hyperspectral data using a Multiple-Endmember Linear Spectral Unmixing Model (MELSUM):

874   Methodology and first results. Planetary and Space Science, 56, 951–975.

875   Dalton, J.B., Prieto-Ballesteros, O., Kargel, J.S., Jamieson, C.S., Jolivet, J., and Quinn, R. (2005)

876   Spectral comparison of heavily hydrated salts with disrupted terrains on Europa. Icarus, 177, 472–

877   490.

878   Dalton, J.B., Shirley, J.H., and Kamp, L.W. (2012) Europa's icy bright plains and dark linea: Exogenic

879   and endogenic contributions to composition and surface properties. Journal of Geophysical

880   Research, 117, E03003.

881   Downs, R.T., Gibbs, G.V., Bartelmehs, K.L., and Boisen, M.B. Jr. (1992) Variations of bond lengths

882   and volumes of silicate tetrahedra with temperature. American Mineralogist, 77, 751–757.

883   Ende, M., Kirkkala, T., Loitzenbauer, M., Talla, D., Miletich, R., and Wildner, M. (2019a) Pressure

884   induced phase transitions of dwornikite. Zeitschrift für Kristallographie Supplement 39, 60–61.

885   Ende, M., Loitzenbauer, M., Matzinger, P., Meusburger, J., Talla, D., Miletich, R., and Wildner, M.

886   (2019b) Pressure induced phase transition in $CoSO_4 \cdot H_2O$. Book of Abstracts of the 32nd European

887   Crystallographic Meeting, 284.

888   Figgis, B.N., and Hitchman, M.A. (2000) Ligand field theory and its applications, 364p. Wiley-VCH,

889   New York.

890   Frederiksson, K., and Kerridge, J.F. (1988) Carbonates and sulphates in C1 chondrites: Formation by

891   aqueous activity on the parent body. Meteoritics, 23, 35–44.

892   Hawthorne, F.C., Groat, L.A., Raudsepp, M., and Ercit, T.S. (1987) Kieserite, $Mg(SO_4)(H_2O)$, a

893   titanite-group mineral. Neues Jahrbuch für Mineralogie Abhandlungen, 157, 121–132.µ

894   Giester, G., and Wildner, M. (1992) The crystal structures of kieserite-group compounds. II. Crystal struc-

895   tures of $Me(II)SeO_4 \cdot H_2O$ (Me = Mg, Mn, Co, Ni, Zn). Neues Jahrbuch für Mineralogie Monatshefte,

896   1992, 135–144.

897   Griffen, D.T., and Ribbe, P.H. (1979) Distortions in the tetrahedral oxyanions of crystalline

898   substances. Neues Jahrbuch Mineralogischer Abhandlungen, 137, 54–73.

899   Jamieson, C.S., Noe Dobrea, E.Z., Dalton, J.B. III, Pitman, K.M., and Abbey, W.Z. (2014) The

900   spectral variability of kieserite ($MgSO_4 \cdot H_2O$) with temperature and grain size and its application to

901   the Martian surface. Journal of Geophysical Research: Planets, 119, 1218–1237.

902   Journaux, B., Daniel, I., Petitgirard, S., Cardon, H., Perrillat, J.-P., Caracas, R., and Mezouar, M.

903   (2017) Salt partitioning between water and high-pressure ices. Implication for the dynamics and

904   habitability of icy moons and water-rich planetary bodies. Earth and Planetary Science Letters,

905   463, 36–47.

906   Kargel, J.S. (1991) Brine volcanism and the interior structures of asteroids and icy satellites. Icarus,

907   94, 368–390.

908   Kargel, J.S., Kaye, J.Z., Head, J.W. III, Marion, G.M., Sassen, R., Crowley, J.K., Prieto-Ballesteros,

909   O., Grant, S.A., and Hogenboom, D.L. (2000) Europa's crust and ocean: Origin, composition, and

910   the prospects for life. Icarus, 148, 226–265.

911   Knauth, L.P., Burt, D.M., and Wohletz, K.H. (2005) Impact origin of sediments at the Opportunity

912   landing site on Mars. Nature, 438, 1123–1128.

913   Lane, M.D. (2007) Mid-infrared emission spectroscopy of sulfate and sulfate-bearing minerals.

914   American Mineralogist, 92, 1–18.

915   Lane, M.D., Bishop, J.L., Dyar, M.D., Hiroi, T., Mertzman, S.A., Bish, D.L., King, P.L., and Rogers,

916   A.D. (2015) Mid-infrared emission spectroscopy and visible/near-infrared reflectance

917   spectroscopy of Fe-sulfate minerals. American Mineralogist, 100, 66–82.

918   Libowitzky, E. (1999) Correlation of O–H stretching frequencies and O–H···O hydrogen bond lengths

919   in minerals. Monatshefte für Chemie, 130, 1047–1059.

920   Lichtenberg, K.A., Arvidson, R.E., Morris, R.V., Murchie, S.L., Bishop, J.L., Fernández-Remolar, D.,

921   Glotch, T.D., Dobrea, E.N., Mustard, J.F., Andrews-Hanna, J. and Roach, L.H. (2010)

922   Stratigraphy of hydrated sulfates in the sedimentary deposits of Aram Chaos, Mars. Journal of

923   Geophysical Research, 115, E00D17.

924   Liu, Y., Glotch, T.D., Scudder, N.A., Kraner, M.L., Condus, T., Arvidson, R.E., Guinness, E.A.,

925   Wolff, M.J., and Smith, M.D. (2016) End-member identification and spectral mixture analysis of

926   CRISM hyperspectral data: A case study on southwest Melas Chasma, Mars. Journal of

927   Geophysical Research: Planets, 121, 2004–2036.

928   Mangold, N., Gendrin, A., Gondet, B., LeMouelic, S., Quantin, C., Ansan, V., Bibring, J.-P.,

929   Langevine, Y., Masson, P., and Nukum, G. (2008) Spectral and geologic study of the sulfate-rich

930   region of West Candor Chasma, Mars. Icarus, 194, 519–543.

931   McCord, T.B., Hansen, G.B., and Hibbits, C.A. (2001) Hydrated salt minerals on Ganymede's surface:

932   Evidence of an ocean below. Science, 292, 1523–1525.

933   McKinnon, W.B., and Zolensky, M.F. (2003) Sulfate content of Europa's ocean and shell:

934   Evolutionary considerations and some geological and astrobiological implications. Astrobiology,

935   3, 879–897.

936   Meusburger, J.M., Ende, M., Talla, D., Miletich, R., and Wildner, M. (2018) Pressure induced second

937   order phase transition in monohydrated magnesium sulphate ($MgSO_4·H_2O$): A new polymorph

938   potentially occurring on icy satellites. Geophysical Research Abstracts 20, 8136.

939   Meusburger, J.M., Ende, M., Talla, D., Wildner, M., and Miletich, R. (2019) Transformation

940   mechanism of the pressure-induced C2/c-to-P$\overline{1}$ transition in ferrous sulphate monohydrate single

941   crystals. Journal of Solid State Chemistry, 277, 240–252.

942   Milton, C., Evans. H.T., and Johnson, R.G. (1982) Dwornikite, $(Ni,Fe)SO_4·H_2O$, a member of the

943   kieserite group from Minasragra, Peru. Mineralogical Magazine 46, 351–355.

944   Nakamura, R., and Ohtani, E. (2011) The high-pressure phase relation of the $MgSO_4–H_2O$ system and

945   its implication for the internal structure of Ganymede. Icarus, 211, 648–654.

946   Noel, A., Bishop, J.L., Al-Samir, M., Gross, C., Flahaut, J., McGuire, P.C., Weitz, C.M., Seelos, F.,

947   and Murchie, S. (2015) Mineralogy, morphology and stratigraphy of the light-toned interior

948   layered deposits at Juventae Chasma. Icarus, 251, 315–331.

949   Pitman, K.M., Noe Dobrea, E.Z., Jamieson, C.S., Dalton, J.B. III, Abbey, W.J., and Joseph, E.C.S.

950   (2014) Reflectance spectroscopy and optical functions for hydrated Fe-sulfates. American

951   Mineralogist, 99, 1593–1603.

952   Powell, R., and Holland, T. (1993) On the formulation of simple mixing models for complex phases.

953   American Mineralogist, 78, 1174–1180.

954   Roach, L.H., Mustard, J.F., Swayze, G., Milliken, R.E., Bishop, J.L., Murchie, S.L., and Lichtenberg,

955   K. (2010) Hydrated mineral stratigraphy of Ius Chasma, Valles Marineris. Icarus, 206, 253–268.

956   Robinson, K., Gibbs, G.V., and Ribbe, P.H. (1971) Quadratic elongation: a quantitative measure of

957   distortion in coordination polyhedra. Science, 172, 567–570.

958   Ruff, S.W., Christensen, P.R., Barbera, P.W., and Anderson, D.L. (1997) Quantitative thermal

959   emission spectroscopy of minerals: A laboratory technique for measurement and calibration.

960   Journal of Geophysical Research, 102, 14899–14913.

961   Shannon, R.D. (1976) Revised effective ionic radii and systematic studies of interatomic distances in

962   halides and chalcogenides. Acta Crystallographica, A32, 751–767.

963   Sheldrick, G.M. (2008) A short history of SHELX. Acta Crystallographica, A64, 112–122.

964   Solomonidou, A., Coustenis, A., Bampasidis, G., Kyriakopoulos, K., Moussas, X., Bratsolis, E., and

965   Hirtzig, M. (2011) Water oceans of Europa and other moons: implications for life in other solar

966   systems. Journal of Cosmology, 13, 4191–4211.

967   Spencer, J.R., Barr, A.C., Esposito, L.W., Helfenstein, P., Ingersoll, A.P., Jaumann, R., McKay, C.P.,

968   Nimmo, F., Porco, C.C., and Waite, J.H. (2009) Enceladus: An active cryovolcanic satellite. In

969   M.K. Dougherty, L.W. Esposito, S.M. Krimigis, Eds., Saturn from Cassini-Huygens, pp 683–724.

970   Springer, Dordrecht Heidelberg London New York.

971   Stoilova, D. (2003) Influence of the crystal field stabilization energy of metal[II] ions on the

972   structural distortion of matrix-isolated SO_4^{2-} guest ions in selenate matrices. Spectrochimica Acta,

973   A60, 2243–2251.

974   Stoilova, D., and Lutz, H.D. (1998) Infrared study of v_{OD} modes in isotopically dilute (HDO) kieserite-

975   group compounds $MXO_4 \cdot H_2O$ (M = Mn, Co, Ni, Zn, and X = S, Se) with matrix-isolated M'^{2+} and

976        $X'O_4^{2-}$ guest ions. Journal of Molecular Structure, 450, 101–106.

977   Stoilova, D., and Lutz, H.D. (2002) Infrared study of the vibrational behaviour of the S-O stretching

978   modes in kieserite-group selenates $MeSeO_4 \cdot H_2O$ with matrix-isolated SO_4^{2-} and Me'^{2+} guest ions

979   (Me = Mn, Co, Ni, Zn). Journal of Molecular Structures, 606, 267–272.

980   Talla, D., and Wildner, M. (2019) Investigation of the kieserite–szomolnokite solid solution series,

981        $(Mg,Fe)SO_4 \cdot H_2O$, with relevance to Mars: a study on crystal chemistry, FTIR- (5200–400 cm^{-1})

982   and Raman- (4000–100 cm^{-1}) spectroscopy under ambient and Martian temperature conditions.

983   American Mineralogist, in press.

984   Vance, S., Bouffard, M., Choukroun, M., and Sotin, C. (2014) Ganymede's internal structure

985   including thermodynamics of magnesium sulfate oceans in contact with ice. Planetary and Space

986   Science, 96, 62–70.

987   van Hinsberg,V.J., Vriend, S.P., and Schumacher, J.C. (2005a) A new method to calculate end-

988   member thermodynamic properties of minerals from their constituent polyhedra I: enthalpy,

989   entropy and molar volume. Journal of Metamorphic Geology, 23, 165–179.

990   van Hinsberg,V.J., Vriend, S.P. , and Schumacher, J.C. (2005b) A new method to calculate end-

991   member thermodynamic properties of minerals from their constituent polyhedra II: heat capacity,

992   compressibility and thermal expansion. Journal of Metamorphic Geology, 23, 681–693.

993   Vegard, L. (1921) Die Konstitution der Mischkristalle und die Raumfüllung der Atome. Zeitschrift der

994   Physik, 5, 17–26.

995   Wildner, M. (1996) Polarized electronic absorption spectra of Co^{2+} ions in the kieserite-group

996   compounds $CoSO_4 \cdot H_2O$ and $CoSeO_4 \cdot H_2O$. Physics and Chemistry of Minerals, 23, 489–496.

997   Wildner, M., and Giester, G. (1991) The crystal structure of kieserite-group compounds. I. Crystal

998   structures of $Me^{(II)}SO_4 \cdot H_2O$ (Me = Mn, Fe, Co, Ni, Zn). Neues Jahrbuch für Mineralogie

999   Monatshefte, 1991, 296–306.

1000   Wildner, M., Beran, A., and Koller, F. (2013) Spectroscopic characterisation and crystal field

1001   calculations of varicoloured kyanites from Loliondo, Tanzania. Mineralogy and Petrology, 107,

1002   289–310.

1003   Witzke, A., Arnold, G., and Stöffler, D. (2007) Spectral detectability of Ca- and Mg-sulphates in

1004   Martian bright soils in the 4-5 μm wavelength range. Planetary and Space Science, 55, 429-440.

1005   Zolotov, M.Y., and Shock, E.L. (2001) Composition and stability of salts on the surface of Europan

1006   and their oceanic origin. Journal of Geophysical Research, 106, 32815–32827.

1007   **Table captions / Tables**

1008

1009

1010   **Table 1.** Composition of the studied samples as shown in Fig. 1, determined by wet chemical

1011   analyses. Deviations of the actual sample Ni content $x_{Ni(sample)}$ from the preset Mg/Ni ratio in

1012   the batch $x_{Ni(preset)}$ are also given. The analytical error amounts to 0.005 wt% for Mg and 0.002

1013   wt% for Ni. Note that the Mg/Ni ratios of individual hand-picked crystals used for the single

1014   crystal X-ray diffraction studies (from 'leaking vessel' runs) were extracted as variable

1015   parameter in the respective structure refinement runs.

1016

Sample ID	Mg (wt%)	Ni (wt%)	$x_{Ni(sample)}$	$x_{Ni(preset)}$	$x_{Ni(sample)}$-$x_{Ni(preset)}$
Ni5a	17.60	0.68	0.016	0.050	-0.034
Ni10a	17.63	1.11	0.025	0.100	-0.075
Ni15a	17.36	1.61	0.037	0.150	-0.113
Ni20a	15.68	2.49	0.062	0.200	-0.138
Ni30a	14.72	3.98	0.101	0.300	-0.199
Ni40a	14.00	6.05	0.152	0.400	-0.248
Ni100a	0.11	27.29	0.990	1.00	0.001
Ni10aq	16.74	3.20	0.073	0.100	-0.027
Ni20aq	14.55	7.77	0.181	0.200	-0.019
Ni30aq	12.32	9.90	0.250	0.300	-0.050
Ni40aq	10.26	13.92	0.360	0.400	-0.040
Ni50aq	8.40	14.48	0.417	0.500	-0.083
Ni60aq	6.55	16.37	0.508	0.600	-0.092
Ni70aq	4.66	21.96	0.661	0.700	-0.039
Ni80aq	3.07	22.92	0.756	0.800	-0.044
Ni90aq	1.47	22.60	0.864	0.900	-0.036
Ni100aq	0.01	27.85	0.999	1.000	-0.001

1017

1018

1019

1020

1021

1022

1023

1024

1025

1026

1027

1028 **Table 2.** Crystal data and details of X-ray data collections and structure refinements for

1029 selected representatives of the $Mg_{1-x}Ni_x(SO_4)\cdot H_2O$ solid solution series. Common data:

1030 monoclinic, space group $C2/c$ (no. 15), $Z = 4$. Respective data for endmember kieserite are

1031 reproduced from Bechtold and Wildner (2016).

1032

$Mg_{1-x}Ni_x(SO_4)\cdot H_2O$	$Mg_{1.00}Ni_{0.00}$	$Mg_{0.76}Ni_{0.24}$	$Mg_{0.48}Ni_{0.52}$	$Mg_{0.24}Ni_{0.76}$	$Mg_{0.00}Ni_{1.00}$
x_{Ni}	0.0	0.236(2)	0.525(2)	0.759(2)	1.0
a (Å)	6.910(1)	6.891(1)	6.859(1)	6.845(1)	6.829(1)
b (Å)	7.634(2)	7.622(1)	7.620(1)	7.614(1)	7.605(1)
c (Å)	7.643(2)	7.592(1)	7.545(1)	7.502(1)	7.463(1)
β (°)	118.00(1)	117.98(1)	117.84(1)	117.80(1)	117.75(1)
V (Å^3)	356.00(14)	352.14(9)	348.67(9)	345.84(9)	342.98(9)
μ (mm^{-1})	0.97	2.16	3.64	4.86	6.14
D_{calc} (gcm^{-3})	2.582	2.763	2.980	3.159	3.346
Exposure time (s)/frame	140	180	60	40	40
CCD frames processed	508	497	505	531	503
Frame scale factors $_{max, min}$	1.11, 0.89	1.16, 0.77	1.21, 0.89	1.20, 0.72	1.18, 0.81
Total number of intensity data	12919	14225	16826	13763	11698
Total number of reflections	8865	8270	7928	8698	8191
Intensity data for unit cell	5101	7662	12062	6952	4887
Number of hkl's	3995	4052	4037	3995	3728
Unique hkl's	1089	1082	1071	1072	1056
R_i (%)	3.20	3.66	2.94	3.53	2.60
$F_o > 4\sigma(F_o)$	937	919	1005	1029	1019
Variables	39	42	42	42	40
wR2 [for all F_o^2] (%)	6.17	7.62	5.03	4.80	4.99
weighting parameters a, b^a	0.028, 0.20	0.021, 0.85	0.019, 0.30	0.024, 0.08	0.024, 0.52
R1 [for $F_o > 4\sigma(F_o)$] (%)	2.27	3.33	2.05	1.91	1.95
R1 [for all F_o] (%)	2.94	4.59	2.28	2.02	2.05
Goodness of fit	1.109	1.170	1.143	1.104	1.077
Extinction coefficient	0	0.002(2)	0.010(2)	0.016(2)	0.023(2)
$\Delta\rho_{max, min}$ (e$^-$ Å^{-3})	0.47, -0.51	0.83, -0.44	1.02, -0.55	1.18, -0.77	0.78, -0.97

1033 ^{a} $w = 1 / [\sigma^2(F_o^2) + (a \times P)^2 + b \times P]$; $P = \{[\text{max of } (0 \text{ or } F_o^2)] + 2F_c^2\} / 3$

1034

1035

1036 **Table 3**. Structure parameters at room temperature for selected representatives of the

1037 $Mg_{1-x}Ni_x(SO_4)\cdot H_2O$ solid solution series. U_{ij} are given in pm^2. Wyckoff positions: Mg/Ni on

1038 4b (sym $\bar{1}$): 0,½,0 etc.; S and O3 on 4e (sym 2): 0,y,¼ etc., $U_{23} = U_{12} = 0$; O1, O2 and H on 8f

1039 (sym 1): x,y,z etc. Respective data for endmember kieserite are given in Bechtold and Wildner

1040 (2016).

$Mg_{1-x}Ni_x(SO_4)\cdot H_2O$		$Mg_{0.76}Ni_{0.24}$	$Mg_{0.48}Ni_{0.52}$	$Mg_{0.24}Ni_{0.76}$	$Mg_{0.00}Ni_{1.00}$
Mg/Ni	x_{Ni}	0.236(2)	0.525(2)	0.759(2)	1.0
	U_{11}	85(2)	69(1)	67(1)	57(1)
	U_{22}	92(2)	86(1)	74(1)	69(1)
	U_{33}	103(2)	84(1)	72(1)	62(1)
	U_{23}	4(1)	3(1)	3(1)	2(1)
	U_{13}	37(2)	29(1)	31(1)	25(1)
	U_{12}	–4(2)	–3(1)	–3(1)	–3(1)
	U_{eq}	96(1)	82(1)	76(1)	64(1)
S	y	0.15535(6)	0.15612(3)	0.15643(3)	0.15664(4)
	U_{11}	71(2)	56(1)	53(1)	44(1)
	U_{22}	89(2)	76(1)	62(1)	59(1)
	U_{33}	111(2)	92(1)	77(1)	67(1)
	U_{13}	36(1)	26(1)	28(1)	23(1)
	U_{eq}	93(1)	78(1)	65(1)	58(1)
O1	x	0.17513(17)	0.17421(10)	0.17356(10)	0.17289(12)
	y	0.04528(15)	0.04590(10)	0.04637 (9)	0.04649(11)
	z	0.39678(17)	0.39953(10)	0.40142(10)	0.40331(12)
	U_{11}	100(4)	82(2)	78(2)	71(2)
	U_{22}	165(4)	160(3)	150(2)	142(3)
	U_{33}	178(5)	164(3)	150(2)	136(3)
	U_{23}	67(4)	68(2)	70(2)	69(2)
	U_{13}	51(3)	42(2)	43(2)	38(2)
	U_{12}	40(3)	37(2)	37(2)	37(2)
	U_{eq}	154(2)	142(1)	130(1)	121(1)
O2	x	0.09460(18)	0.09821(10)	0.10079(10)	0.10307(12)
	y	0.26806(14)	0.26909 (9)	0.26961 (8)	0.26994 (9)
	z	0.15065(17)	0.15246(10)	0.15372(10)	0.15466(11)
	U_{11}	133(4)	118(2)	127(2)	95(2)
	U_{22}	125(4)	117(2)	114(2)	95(2)
	U_{33}	186(5)	164(3)	170(3)	135(3)
	U_{23}	49(3)	43(2)	51(2)	43(2)
	U_{13}	94(4)	82(2)	94(2)	71(2)
	U_{12}	11(3)	14(2)	16(2)	14(2)
	U_{eq}	140(2)	127(1)	113(1)	101(1)
O3	y	0.63411(21)	0.63291(12)	0.63209(11)	0.63135(13)
	U_{11}	104(6)	98(3)	91(3)	79(3)
	U_{22}	140(6)	123(3)	109(3)	103(3)
	U_{33}	131(6)	108(3)	94(3)	82(3)
	U_{13}	52(5)	47(3)	45(2)	37(3)
	U_{eq}	126(3)	110(1)	97(1)	88(1)
H	x	0.092(4)	0.111(3)	0.111(3)	0.108(4)
	y	0.688(4)	0.700(3)	0.695(3)	0.694(3)
	z	0.286(4)	0.294(3)	0.291(3)	0.296(3)
	U_{iso}	262(68)	334(50)	196(40)	201(50)

1041 **Table 4.** Crystal data and details of selected temperature-dependent X-ray data collections

1042 and structure refinements for dwornikite, $Ni(SO_4)\cdot H_2O$. Common data: monoclinic, space

1043 group $C2/c$ (no. 15), $Z = 4$; each 930 CCD frames measured; exposure time/frame 10 s; 40

1044 variables. Respective temperature-dependent data for endmember kieserite are given in Talla

1045 and Wildner (2019), its room temperature data in Bechtold and Wildner (2016), and those for

1046 dwornikite in Table 2.

$Ni(SO_4)\cdot H_2O$	0 °C	−80 °C	−160 °C
a (Å)	6.825(1)	6.812(1)	6.804(1)
b (Å)	7.607(1)	7.612(1)	7.618(1)
c (Å)	7.459(1)	7.444(1)	7.437(1)
β (°)	117.72(1)	117.63(1)	117.58(1)
V (Å^3)	342.79	341.98	341.66
μ (mm$^{-1)}$)	6.14	6.16	6.16
D_{calc} (gcm^{-3})	3.348	3.356	3.359
Frame scale factors $_{max,\ min}$	0.75, 0.64	0.75, 0.66	0.75, 0.66
Total number of reflections	11574	11491	11115
Intensity data for unit cell	8253	8457	8497
Unique hkl's	1064	1063	1061
R_i (%)	2.40	2.32	2.35
$F_o > 4\sigma(F_o)$	1031	1036	1034
wR2 [for all F_o^2] (%)	4.11	4.20	4.22
weighting parameters a, b^a	0.021, 0.34	0.021, 0.47	0.021, 0.53
R1 [for $F_o > 4\sigma(F_o)$] (%)	1.54	1.60	1.61
R1 [for all F_o] (%)	1.62	1.67	1.66
Goodness of fit	1.127	1.118	1.123
Extinction coefficient	0.025(1)	0.021(1)	0.019(1)
$\Delta\rho_{max,\ min}$ (e$^-$ Å^{-3})	0.67, -0.68	0.80, -0.72	0.82, -0.67

1047 ^{a} $w = 1 / [\sigma^2(F_o^2) + (a\times P)^2 + b\times P]$; $P = \{[\text{max of } (0 \text{ or } F_o^2)] + 2F_c^2\} / 3$
1048
1049
1050
1051
1052
1053
1054
1055
1056
1057 **Table 5.** Selected temperature-dependent structure parameters for dwornikite, $Ni(SO_4)\cdot H_2O$.

1058 U_{ij} are given in pm^2. Wyckoff positions: Ni on 4b (sym $\bar{1}$): 0,½,0 etc.; S and O3 on 4e (sym

1059 2): 0,y,¼ etc., $U_{23} = U_{12} = 0$; O1, O2 and H on 8f (sym 1): x,y,z etc. Respective room-

1060 temperature data are given in Table 3.

1061

$Ni(SO_4) \cdot H_2O$		0 °C	−80 °C	−160 °C
Ni	U_{11}	52(1)	39(1)	27(1)
	U_{22}	63(1)	47(1)	32(1)
	U_{33}	55(1)	41(1)	28(1)
	U_{23}	2(1)	2(1)	1(1)
	U_{13}	22(1)	17(1)	13(1)
	U_{12}	−2(1)	−1(1)	−1(1)
	U_{eq}	58(1)	43(1)	29(1)
S	y	0.15681(3)	0.15727(3)	0.15763(4)
	U_{11}	40(1)	31(1)	23(1)
	U_{22}	54(1)	42(1)	30(1)
	U_{33}	60(1)	45(1)	32(1)
	U_{13}	20(1)	16(1)	12(1)
	U_{eq}	53(1)	40(1)	28(1)
O1	x	0.17279(10)	0.17262(10)	0.17257(10)
	y	0.04668(9)	0.04732(9)	0.04772(9)
	z	0.40353(10)	0.40413(10)	0.40473(9)
	U_{11}	65(2)	52(2)	39(2)
	U_{22}	132(3)	100(2)	70(2)
	U_{33}	125(2)	94(2)	67(2)
	U_{23}	63(2)	46(2)	32(2)
	U_{13}	36(2)	28(2)	20(2)
	U_{12}	32(2)	25(2)	18(2)
	U_{eq}	111(1)	84(1)	60(1)
O2	x	0.10339(10)	0.10428(10)	0.10507(10)
	y	0.27006(8)	0.27059(8)	0.27108(8)
	z	0.15477(9)	0.15519(9)	0.15552(9)
	U_{11}	89(2)	67(2)	51(2)
	U_{22}	86(2)	66(2)	47(2)
	U_{33}	122(2)	94(2)	67(2)
	U_{23}	38(2)	26(2)	18(2)
	U_{13}	66(2)	51(2)	38(2)
	U_{12}	12(2)	7(2)	3(2)
	U_{eq}	93(1)	70(1)	51(2)
O3	y	0.63108(12)	0.63077(12)	0.63055(12)
	U_{11}	76(3)	60(3)	42(3)
	U_{22}	92(3)	70(3)	56(3)
	U_{33}	76(3)	61(3)	50(3)
	U_{13}	37(2)	29(2)	22(2)
	U_{eq}	81(1)	63(1)	49(1)
H	x	0.108(3)	0.109(3)	0.109(3)
	y	0.695(2)	0.695(3)	0.695(3)
	z	0.294(3)	0.294(3)	0.294(3)
	U_{iso}	197(43)	204(48)	200(50)

1062

1063 **Table 6.** Survey of crystal chemical data for selected representatives of the

1064 $Mg_{1-x}Ni_x(SO_4)\cdot H_2O$ solid solution series: bond lengths (Å) and angles (°), polyhedral volumes

1065 ($Å^3$), bond strengths (without H atoms; calculated according to Brese & O'Keeffe, 1991), and

1066 polyhedral distortion parameters (Brown & Shannon, 1973; Robinson *et al.*, 1971; Griffen &

1067 Ribbe, 1979). Data for endmember kieserite are reproduced from Bechtold and Wildner

1068 (2016).

1069

$Mg_{1-x}Ni_x(SO_4)\cdot H_2O$	$Mg_{1.00}Ni_{0.00}$	$Mg_{0.76}Ni_{0.24}$	$Mg_{0.48}Ni_{0.52}$	$Mg_{0.24}Ni_{0.76}$	$Mg_{0.00}Ni_{1.00}$
x_{Ni}	0.0	0.236(2)	0.525(2)	0.759(2)	1
Me–O1 (2×)	2.0216(7)	2.0245(11)	2.0267(7)	2.0304(7)	2.0334(8)
Me–O2 (2×)	2.0414(7)	2.0393(11)	2.0370(7)	2.0349(6)	2.0327(7)
Me–O3 (2×)	2.1714(6)	2.1558(8)	2.1409(5)	2.1281(5)	2.1162(5)
<Me–O>	2.0782	2.0732	2.0682	2.0645	2.0608
$\Delta_{oct}\times10^3$	1.023	0.802	0.622	0.476	0.362
Σ v.u. (Me)	2.15	2.12	2.08	2.04	2.01
O1–Me–O2 (2×) [a]	85.91(3)	85.77(5)	85.52(3)	85.35(3)	85.15(3)
O1–Me–O3 (2×) [a]	88.50(2)	87.98(3)	87.56(2)	87.18(2)	86.79(2)
O2–Me–O3 (2×) [a]	87.20(3)	87.17(5)	87.30(3)	87.28(3)	87.26(2)
σ_{oct}^2	9.75	10.90	12.11	13.44	15.03
V_{oct}	11.901(10)	11.814(11)	11.727(7)	11.660(7)	11.592(8)
S–O1 (2×)	1.4639(7)	1.4629(11)	1.4652(7)	1.4646(6)	1.4651(7)
S–O2 (2×)	1.4817(7)	1.4810(11)	1.4830(6)	1.4850(6)	1.4868(7)
<S–O>	1.4728	1.4720	1.4741	1.4748	1.4760
BLDP×10³	6.98	7.10	6.99	7.99	8.49
Σ v.u. (S)	6.02	6.03	6.00	5.99	5.97
O1–S–O1'	109.94(6)	110.01(9)	110.05(6)	110.19(6)	110.26(7)
O1–S–O2 (2×)	108.59(4)	108.53(6)	108.59(4)	108.46(3)	108.43(4)
O1–S–O2'(2×)	110.41(4)	110.34(7)	110.29(4)	110.34(4)	110.28(4)
O2–S–O2'	108.89(6)	109.09(9)	109.03(6)	109.05(5)	109.16(6)
σ_{tetr}^2	0.77	0.74	0.68	0.85	0.84
V_{tetr}	1.639(2)	1.636(3)	1.643(2)	1.646(2)	1.650(2)
Me–O1–S	140.38(4)	139.44(7)	138.34(4)	137.62(4)	136.82(5)
Me–O2–S	134.31(4)	133.42(7)	132.42(4)	131.63(4)	130.89(4)
Me–O3–Me	123.27(5)	123.39(7)	123.53(4)	123.59(4)	123.67(5)
Σ v.u. (O1)	1.95	1.94	1.92	1.91	1.90
Σ v.u. (O2)	1.86	1.85	1.84	1.82	1.81
Σ v.u. (O3)	0.55	0.56	0.56	0.57	0.57
O3···O2	2.7449(8)	2.7273(13)	2.7052(8)	2.6913(8)	2.6774(9)
O3–H	0.81(2)	0.69(3)	0.84(2)	0.83(2)	0.81(2)
O2···H	2.01(2)	2.07(3)	1.92(2)	1.90(2)	1.92(2)
O3–H···O2	151(2)	158(3)	155(2)	159(2)	156(2)

1070 [a] plus corresponding obtuse angles

1071 **Table 7.** Survey of selected temperature-dependent crystal chemical data for dwornikite,

1072 $Ni(SO_4) \cdot H_2O$: bond lengths (Å) and angles (°), polyhedral volumes (Å^3), bond strengths

1073 (without H atoms, calculated according to Brese and O'Keeffe 1991), and polyhedral

1074 distortion parameters (Brown and Shannon 1973; Robinson et al. 1971; Griffen and Ribbe

1075 1979). Respective room-temperature data are given in Table 6, those for endmember kieserite

1076 in Bechtold and Wildner (2016); temperature-dependent data for kieserite are given in Talla

1077 and Wildner (2019).

1078

$Ni(SO_4) \cdot H_2O$	0 °C	–80 °C	–160 °C
Ni–O1 (2×)	2.0338(7)	2.0336(7)	2.0336(7)
Ni–O2 (2×)	2.0328(6)	2.0317(6)	2.0309(6)
Ni–O3 (2×)	2.1145(5)	2.1106(5)	2.1085(5)
<Ni–O>	2.0604	2.0586	2.0577
$\Delta_{oct} \times 10^3$	0.345	0.319	0.305
Σ v.u. (Ni)	2.01	2.02	2.02
O1-Ni-O2 (2×) [a]	85.15(3)	85.15(3)	85.13(3)
O1-Ni-O3 (2×) [a]	86.78(2)	86.82(2)	86.81(2)
O2-Ni-O3 (2×) [a]	87.28(3)	87.31(3)	87.33(3)
σ_{oct}^2	15.01	14.86	14.92
V_{oct}	11.585(7)	11.557(7)	11.540(7)
S–O1 (2×)	1.4654(6)	1.4657(7)	1.4672(7)
S–O2 (2×)	1.4869(6)	1.4872(6)	1.4888(6)
<S–O>	1.47615	1.47645	1.4780
BLDP×10^3	8.41	8.41	8.44
Σ v.u. (S)	5.97	5.96	5.94
O1–S–O1'	110.26(6)	110.36(6)	110.41(6)
O1–S–O2 (2×)	108.44(3)	108.45(4)	108.46(4)
O1–S–O2' (2×)	110.25(4)	110.24(4)	110.23(4)
O2–S–O2'	109.19(5)	109.10(5)	109.04(5)
σ_{tetr}^2	0.81	0.84	0.85
V_{tetr}	1.650(2)	1.651(2)	1.657(2)
Ni–O1–S	136.75(4)	136.63(4)	136.47(4)
Ni–O2–S	130.79(4)	130.57(4)	130.38(4)
Ni–O3–S	123.73(4)	123.72(4)	123.72(4)
Σ v.u. (O1)	1.89	1.89	1.89
Σ v.u. (O2)	1.81	1.81	1.80
Σ v.u. (O3)	0.58	0.58	0.59
O3···O2	2.6760(8)	2.6706(8)	2.6667(8)
O3–H	0.81(2)	0.82(2)	0.82(2)
O2···H	1.91(2)	1.90(2)	1.89(2)
O3–H···O2	156 (2)	157(2)	157(2)

1079 [a] plus corresponding obtuse angles

1080 **Table 8.** Wavenumber positions of relevant absorption phenomena in FTIR spectra in each

1081 measuring mode for the kieserite and dwornikite endmembers, Mg/Ni(SO$_4$)·H$_2$O, at room

1082 temperature. Linear regression coefficients of the correlation between the wavenumber

1083 position of each absorption feature and the Ni-content (x_{Ni}) are listed. Positions of weak yet

1084 important bands observed in the region of H$_2$O combination modes are given in the scope of

1085 DRIFT measurements on undiluted sample material.

Transmission (1:300 sample dilution in KBr)

Vibration	Wavenumber position (cm^{-1})		Linear regression coefficients[†]	
	kieserite	dwornikite	a	b
Peak 900	884(1)	941(2)	52(3)	887(1)
$\nu_{1(SO_4)}$	1043(1)	1019(1)	-26(2)	1041(1)
$\nu_{3(SO_4)center}$	1165(1)	1135(1)	-24(3)	1164(1)
$\nu_{2(H_2O)}$	1525(4)	1522(2)	-4(1)	1526(1)
$\nu_{1(H_2O)}$	3182(4)	3057(5)	-134(7)	3191(3)
$\nu_{3(H_2O)}$	3367(12)	3262(21)	-117(12)	3364(5)

Attenuated Total Reflectance (ATR)

Vibration	Wavenumber position (cm^{-1})		Linear regression coefficients[†]	
	kieserite	dwornikite	a	b
Peak 900	866(3)	904(6)	35(4)	860(2)
$\nu_{2(H_2O)}$	1520(1)	1517(2)	-3(4)	1520(1)
$\nu_{1(H_2O)}$	3165(4)	3037(5)	-127(3)	3163(1)
$\nu_{3(H_2O)}$	3345(8)	3292(22)	-37(6)	3347(3)

Diffuse Reflectance (1:20 sample dilution in KBr)

Vibration	Wavenumber position (cm^{-1})		Linear regression coefficients[†]	
	kieserite	dwornikite	a	b
Peak 900	886(3)	938(2)	53(2)	890.6(8)
$\nu_{1(SO_4)}$	1044(2)	1020(1)	-26.6(9)	1044(1)
$\nu_{3(SO_4)center}$	1172(3)	1143(4)	-24(3)	1166(2)
$\nu_{2(H_2O)}$	1523(1)	1521(1)	2.8(4)	1523(1)
$\nu_{1(H_2O)}$	3180(2)	3062(8)	-121(5)	3188(3)
$\nu_{3(H_2O)}$	3365(13)	3265(20)	-88(5)	3353(3)

Diffuse Reflectance (non-diluted sample)

Vibration	Wavenumber position (cm^{-1})		Linear regression coefficients[†]	
	kieserite	dwornikite	a	b
Peak 600	690(1)	696(2)	8(1)	687.4(6)
Reststrahlenband	1316(6)	1286(3)	-31(4)	1310(2)
$\nu_{2(H_2O)}$	1526(3)	1525(1)	-1.4(9)	1527(1)
$\nu_{1(H_2O)}$	3203(20)	3099(6)	-107(4)	3207(2)
$\nu_{3(H_2O)}$	3412(23)	3314(19)	-129(48)	3432(22)
Peak 4700 cm^{-1}	4688(4)	4566(4)	-123(4)	4690(2)
Peak 4850 cm^{-1}	4845(3)	4735(5)	-92(6)	4830(3)
Peak 5090 cm^{-1}	5087(10)	5110(25)	13(7)	5085(3)

1086 [†]Linear regression equation $y = \mathbf{a}(x_{Ni}) + \mathbf{b}$, where y denotes the wavenumber position of the
1087 vibration mode
1088

1089   **Table 9.** Positions of relevant bands in Raman spectra for the kieserite and dwornikite

1090   endmembers, Mg/Ni$(SO_4)\cdot H_2O$. Linear regression coefficients of the correlation between the

1091   band position and the Ni-content (x_{Ni}) are listed. Additionally, changes in the band position

1092   with decreasing temperature are given for all relevant Raman bands.

1093

Peak assignment	Raman shift position at RT (cm^{-1})		Linear regression coefficients[a]		Band shift with temperature decrease ($\times 10^{-2}$ cm^{-1} / °C)
	kieserite	dwornikite	a	b	
Lattice modes	125.3(1)	136.7(8)	12.4(8)	124.3(4)	0.026
$\nu_{transl\ Fe-H_2O}$	219.2(1)	245.57(7)	26(1)	219.6(6)	0.013
$\nu_{2(SO_4)}\_1$	432.2(1)	418.75(6)	-13.8(6)	432.6(3)	-0.004
$\nu_{2(SO_4)}\_2$	502.1(1)	519.0(5)	16.8(6)	501.7(3)	0.019
$\nu_{4(SO_4)}\_1$	628.7(4)	622.0(2)	-7.1(4)	628.2(2)	0.006
$\nu_{4(SO_4)}\_2$	633.8(2)	629.7(1)	-3.5(3)	633.0(1)	-0.003
$\nu_{1(SO_4)}$	1041.8(1)	1020.88(1)	-23(1)	1042(1)	-0.003
$\nu_{3(SO_4)}\_1$	1101.6(1)	1076.06(6)	-27(1)	1101(1)	-0.012
$\nu_{3(SO_4)}\_2$	1118.9(1)	1093.87(4)	-27(1)	1119(1)	0.011
$\nu_{3(SO_4)}\_3$	1216.7(1)	1197.69(7)	-20.4(9)	1216(1)	0.061
$\nu_{2(H_2O)}$	1508.3(1)	1501.2(8)	8(5)	1496(2)	0.018
$\nu_{1(H_2O)}$	3178(2)	3071(5)	-101(7)	3179(3)	-0.481
$\nu_{3(H_2O)}$	3388(4)	3257(25)	-82(9)	3361(4)	0.162[b]

1094   [a]Linear regression equation $y = a(x_{Ni}) + b$, where y denotes the Raman shift position
1095   [b]high uncertainty
1096
1097
1098
1099
1100
1101
1102
1103
1104
1105
1106
1107
1108
1109
1110

1111   **Table 10.** Summary of results from classical crystal field (CF) and superposition model (SM)

1112   calculations for Ni^{2+} in dwornikite, based on observed transitions energies as indicated in Fig.

1113   13. Fixed SM parameters are $R_0 = 2.06$ Å, $t_2 = 3$. All given values are in cm^{-1} except the

1114   nephelauxetic ratio β. Racah B_0 is taken from Figgis and Hitchman (2000).

1115

Szomolnokite	SM (triclinic)	'classical' CF (tetragonal)
Dq_{cub}	–	810
Dq_{eq}	–	804
Dt	–	$-10^{\dagger}$
Ds	–	-120
Racah B	920	920
Racah C	4.2B*	3860
β ($B_0 = 1042$ cm^{-1})	0.88	0.88
Dq_{cub} (from s_4)	813	810
$\bar{B}_4$	4920	–
t_4	$0.8^{\dagger}$	–
$\bar{B}_2$	$250^{\dagger}$	–
s_4	7448	7424
s_2	51	376

1116   * fixed
1117 † see text
1118

1119

1120

1121

1122

1123

1124

1125

1126

1127

1128

1129

1130

1131   **Figures and Figure captions**

1132

1133   **Figure 1.** Deviations between actual Ni-content of the $Mg_{1-x}Ni_x(SO_4)\cdot H_2O$ solid solution

1134   samples used for spectroscopic investigations $x_{Ni(sample)}$ as determined by the wet chemical

1135   analyses and the preset Mg/Ni ratio in the batch $x_{Ni(preset)}$. Errors are equal or smaller than the

1136   symbol size. Note the strong Ni deficiency in the product with the hydrothermal technique in

1137   use (tightly sealed autoclave). This deviation led to the use the 'leaking vessel approach' for

1138   synthesis of single crystals (not depicted), with the actual x_{Ni} ratio refined from the single-

1139   crystal X-ray diffraction results.

1140
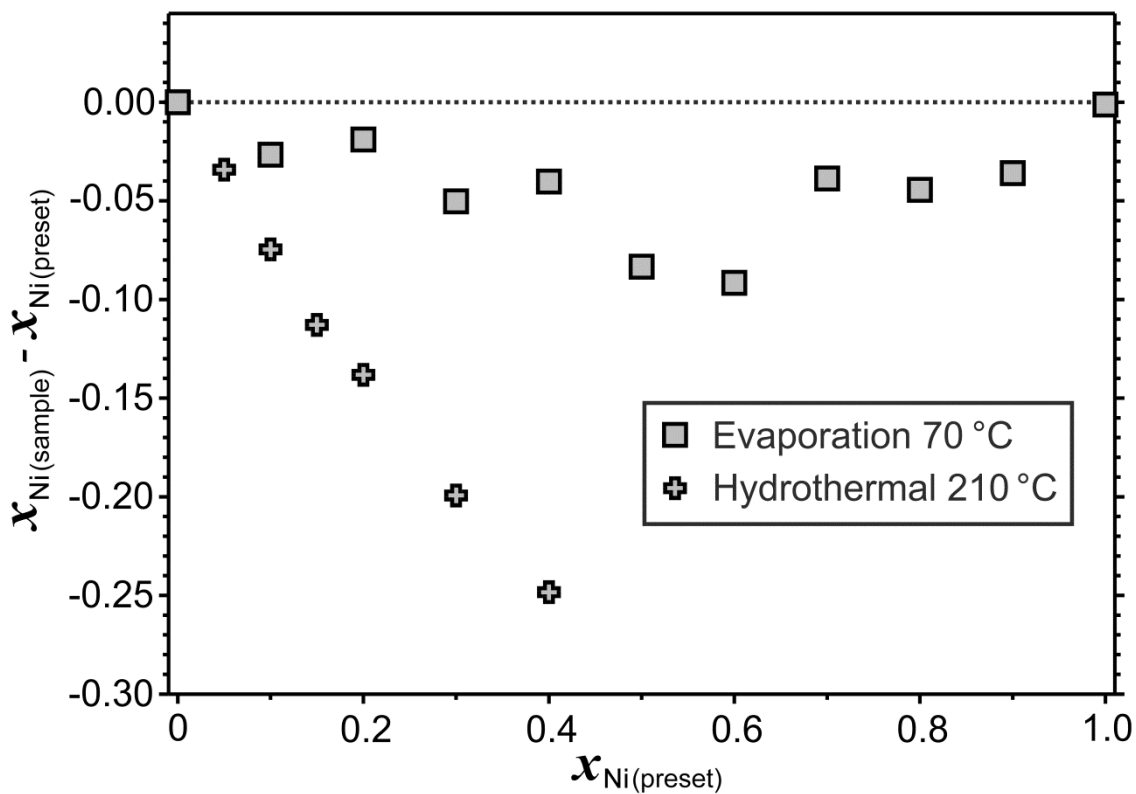
1141

1142

1143

1144

1145

1146

1147

1148   **Figure 2.** Variation of the lattice parameters (**a**) a, b, c and (**b**) β and V along the

1149 $Mg_{1-x}Ni_x(SO_4) \cdot H_2O$ solid solution series with linear regression lines. Errors are equal or

1150   smaller than the symbol size. The data for endmember kieserite are taken from Bechtold and

1151   Wildner (2016). Previous data for dwornikite (Wildner and Giester 1991) are shown (without

1152   errors) as dotted diamond symbols.
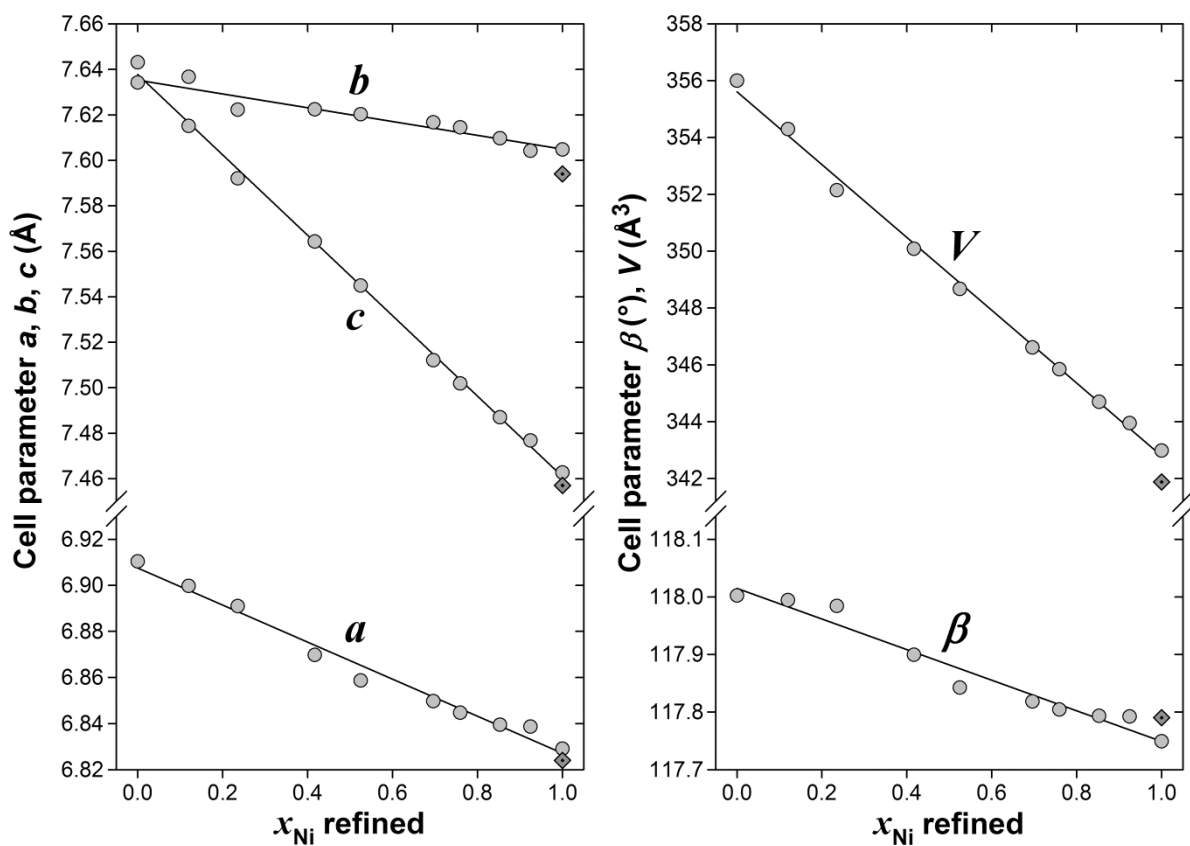
1153

1154

1155

1156

1157

1158

1159

1160

1161

1162

1163   **Figure 3.** Polyhedral geometries along the $Mg_{1-x}Ni_x(SO_4) \cdot H_2O$ solid solution series with

1164   linear regression lines; (**a**) octahedral Me–O bond lengths and (**b**) O–Me–O angles, (**c**)

1165   tetrahedral S–O bond lengths and (**d**) O–S–O angles, where Me represents the metal cation. If

1166   not indicated, errors are equal or smaller than the symbol size. The data for endmember

1167   kieserite are taken from Bechtold and Wildner (2016). Previous data for dwornikite (Wildner

1168   and Giester 1991) are shown (without errors) as dotted diamond symbols.
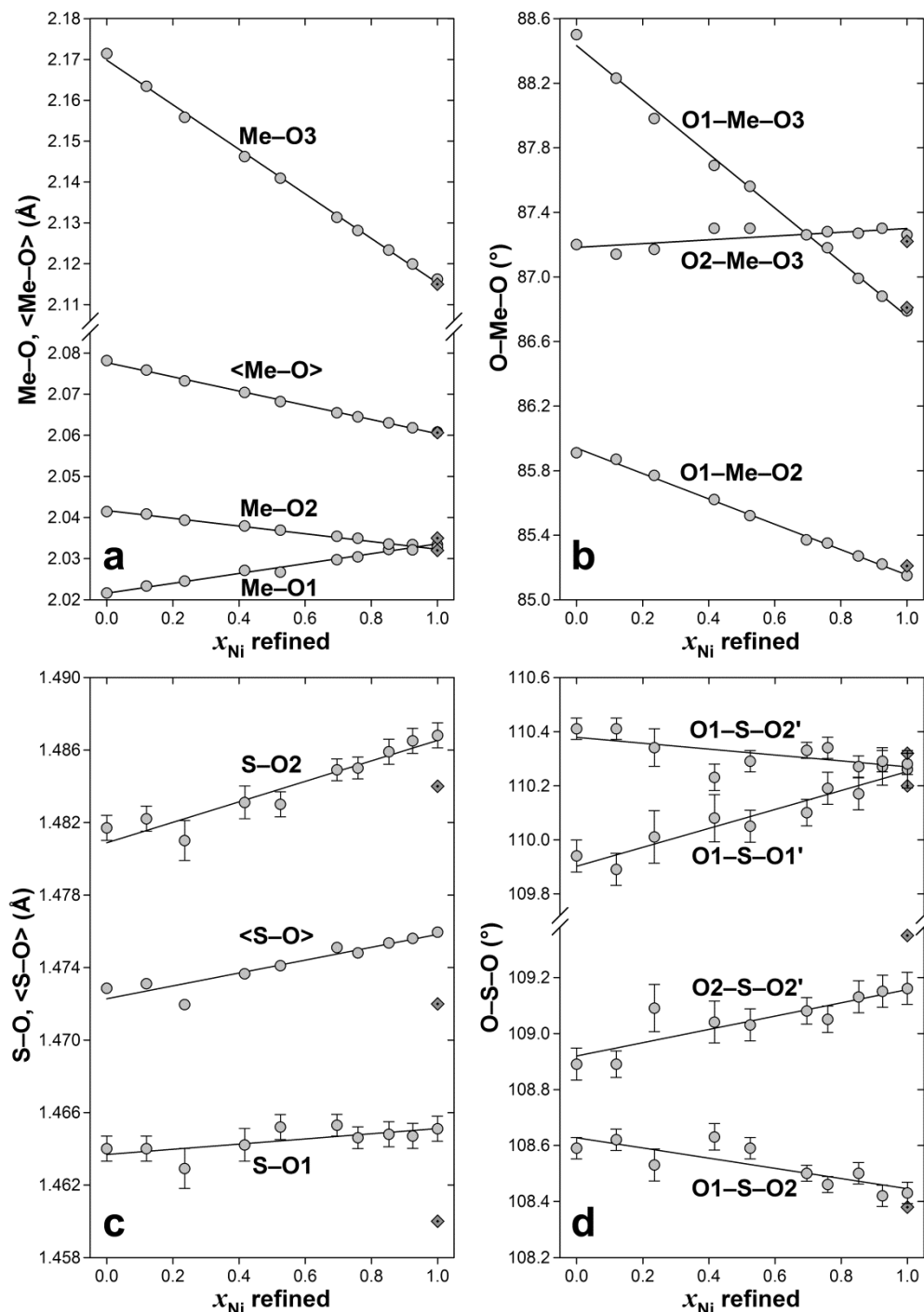
1169

Figure 4. (**a**) Polyhedral volumes, (**b**) Me–O–S and Me–O–Me angles and (**c**) hydrogen bond

lengths along the $Mg_{1-x}Ni_x(SO_4) \cdot H_2O$ solid solution series with linear regression lines. For

(**a**), note the strongly different scales for the tetrahedral and octahedral volumes. If not

indicated, errors are equal or smaller than the symbol size. The data for endmember kieserite

are taken from Bechtold and Wildner (2016). Previous data for dwornikite (Wildner and

Giester 1991) are shown (without errors) as dotted diamond symbols.

1176
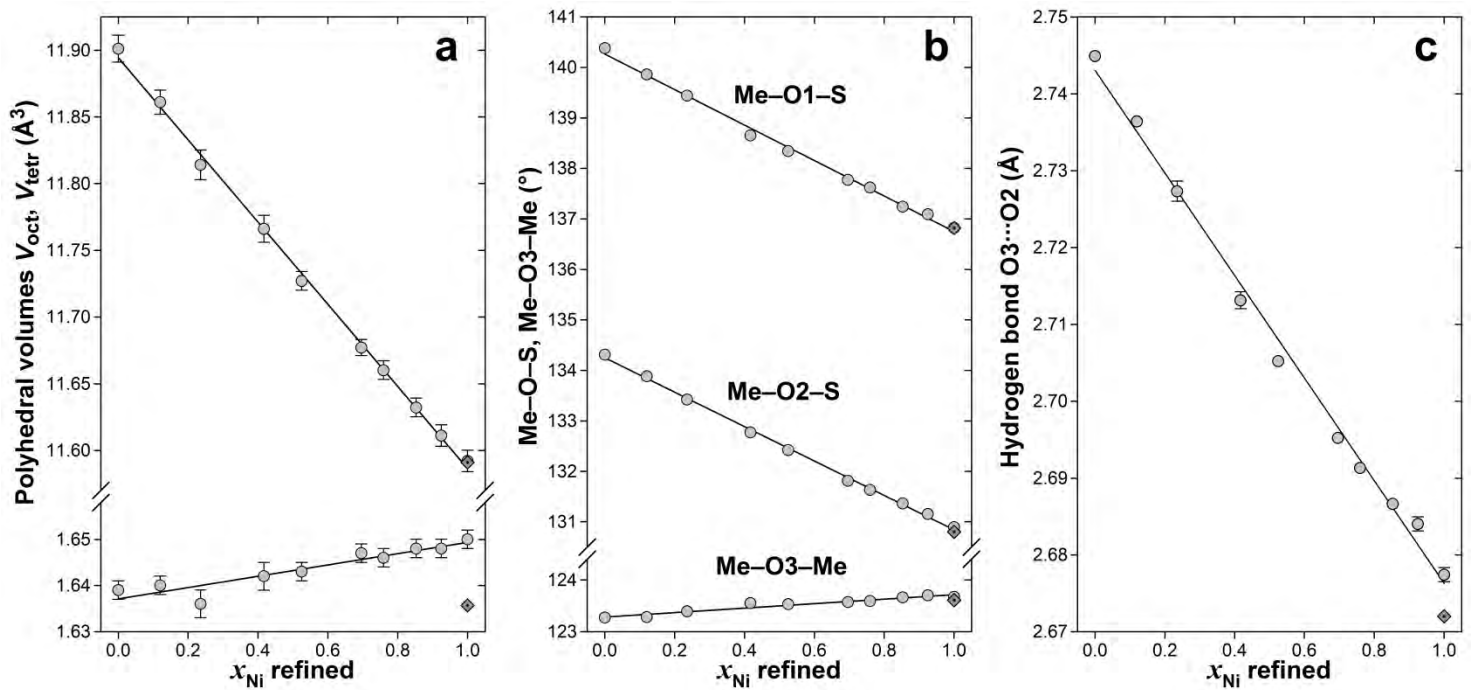
1187

1188

1189

1190

1191

1192

1193

1194

1195 **Figure 5.** Variation of the lattice parameters (**a**) *a*, *b*, *c* and (**b**) *β* and *V*, as well as (**c**)

1196 polyhedral volumes (*V*$_{tetr}$ not corrected for thermal motion) for dwornikite within the

1197 investigated temperature range, with second-order regression lines. If not indicated, errors are

1198 equal or smaller than the symbol size. For (**c**), note the somewhat different scales for the

1199 tetrahedral and octahedral volumes.

1200

1201

1202
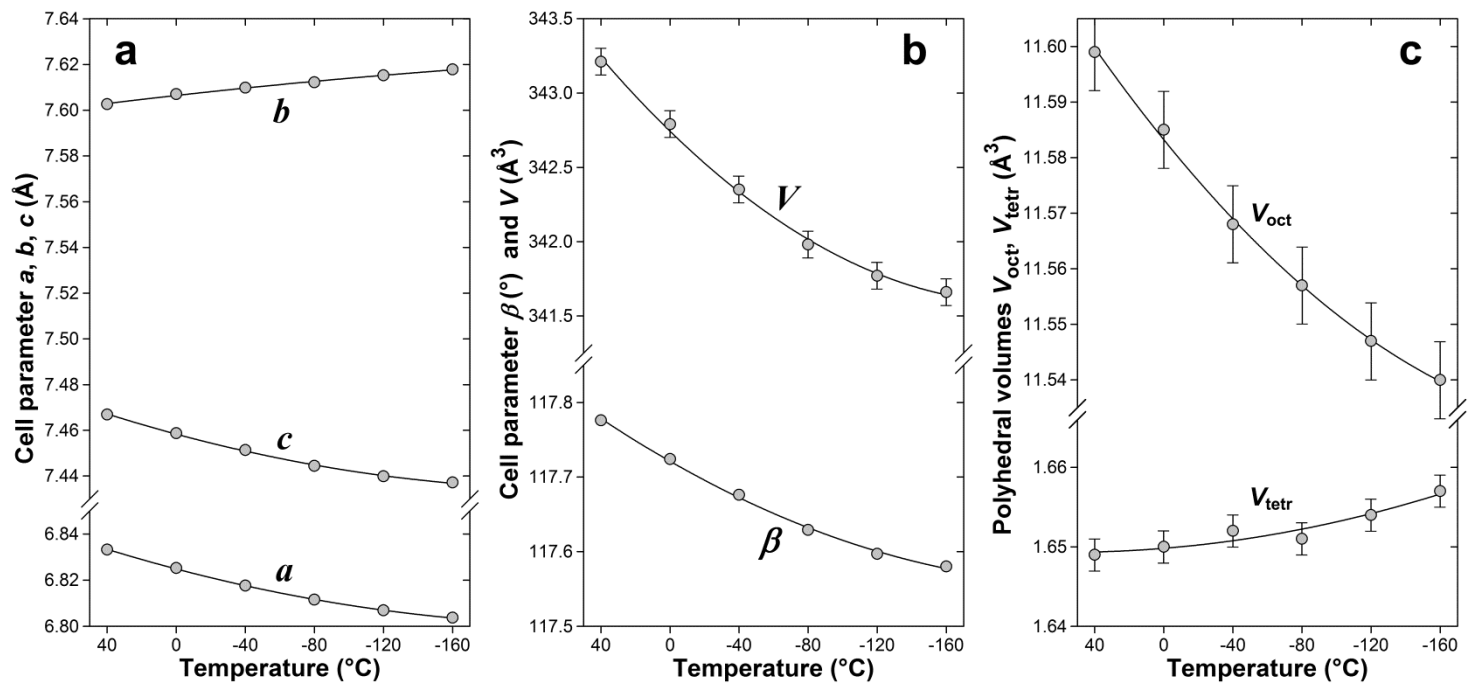
1212

1213

1214

1215

1216

1217

1218

1219

1220

1221 **Figure 6.** Variation of the polyhedral geometries (**a**) octahedral Me–O bond lengths and (**b**)

1222 O–Me–O angles, (**d**) tetrahedral S–O bond lengths (uncorrected for thermal motion) and (**e**)

1223 O–S–O angles, as well as of (*c*) Ni–O–S and Ni–O–Ni angles and (**f**) the hydrogen bond

1224 length in dwornikite within the investigated temperature range, with second-order regression

1225 lines. If not indicated, errors are equal or smaller than the symbol size.

1226

12
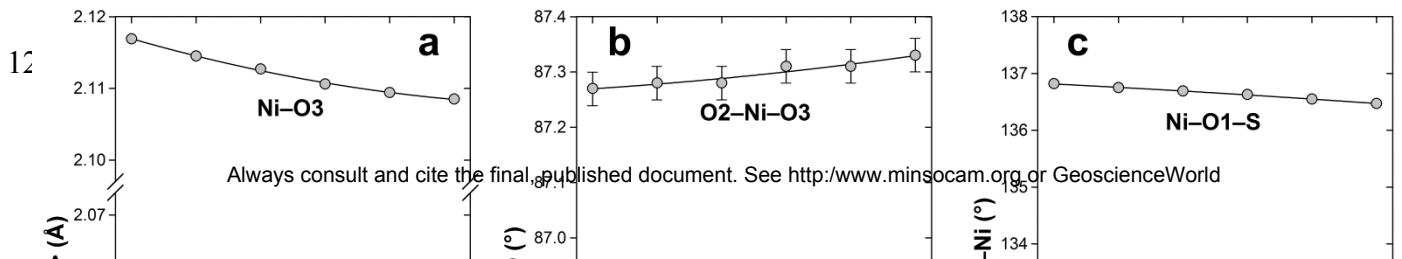
1228

1229

1230

1231

1232

1233

1234

1235

1236

1237

1238

1239

1240

1241

1242

1243

1244

1245

1246

1247 **Figure 7.** FTIR spectra of kieserite (Mg) and dwornikite (Ni) in each measuring mode. In

1248 addition to band position changes between the endmembers, note the differences in band

1249 positions and shapes between the various measuring modes. Data for kieserite are taken from

1250 Talla and Wildner (2019).
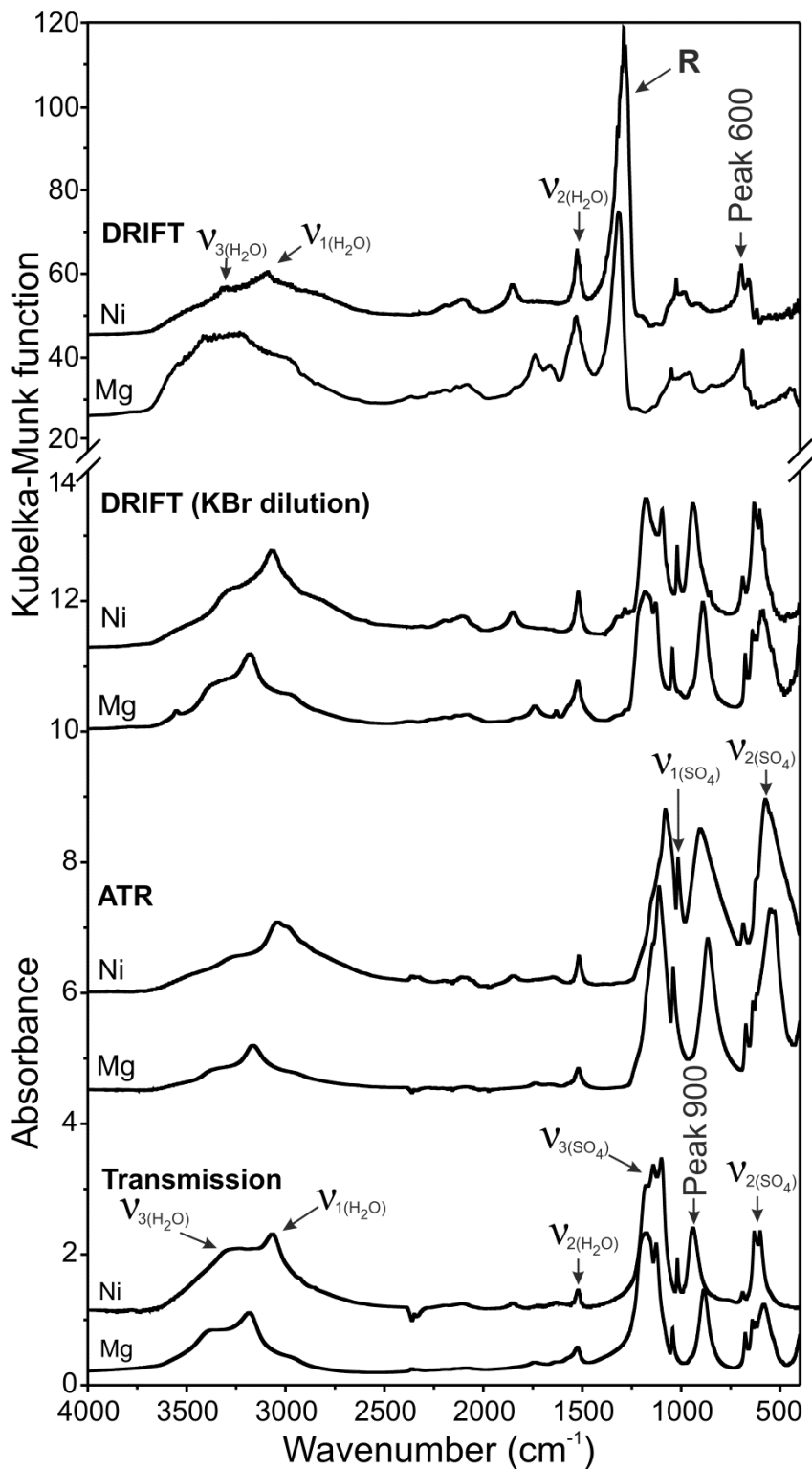
1251

Figure 8. Spectral region with three diagnostic H_2O combination modes, (**a**) observed in

DRIFT measurements of kieserite (from Talla and Wildner 2019) and dwornikite on undiluted

sample material, (**b**) detailed plot of band position change for the examined bands across the

1255   kieserite-dwornikite solid solution series. Errors equal or smaller than the symbol size are not

1256   plotted.
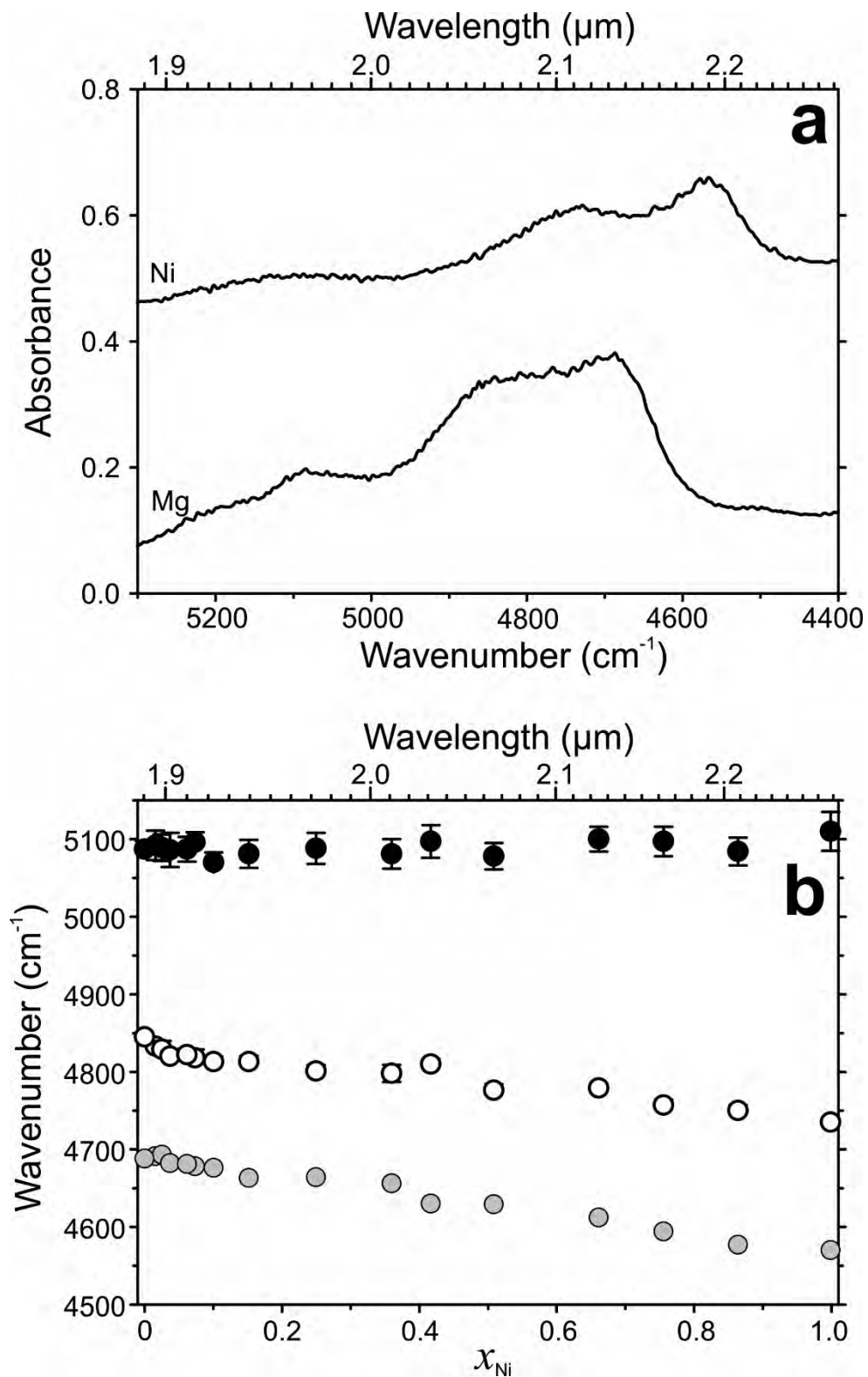
1257

Figure 9. Dependence of the positions of relevant FTIR absorption features (transmission

measurements) of the $Mg_{1-x}Me_x(SO_4)\cdot H_2O$ solid solutions (**a**) on the Ni-content and (**b**) on the

1260   Fe-content at room temperature (RT). Data for the Mg-Fe solid solution are taken from Talla

1261   and Wildner (2019). Note the opposite trends in the H_2O-related modes. Errors equal or

1262   smaller than the symbol size are not plotted.

1263
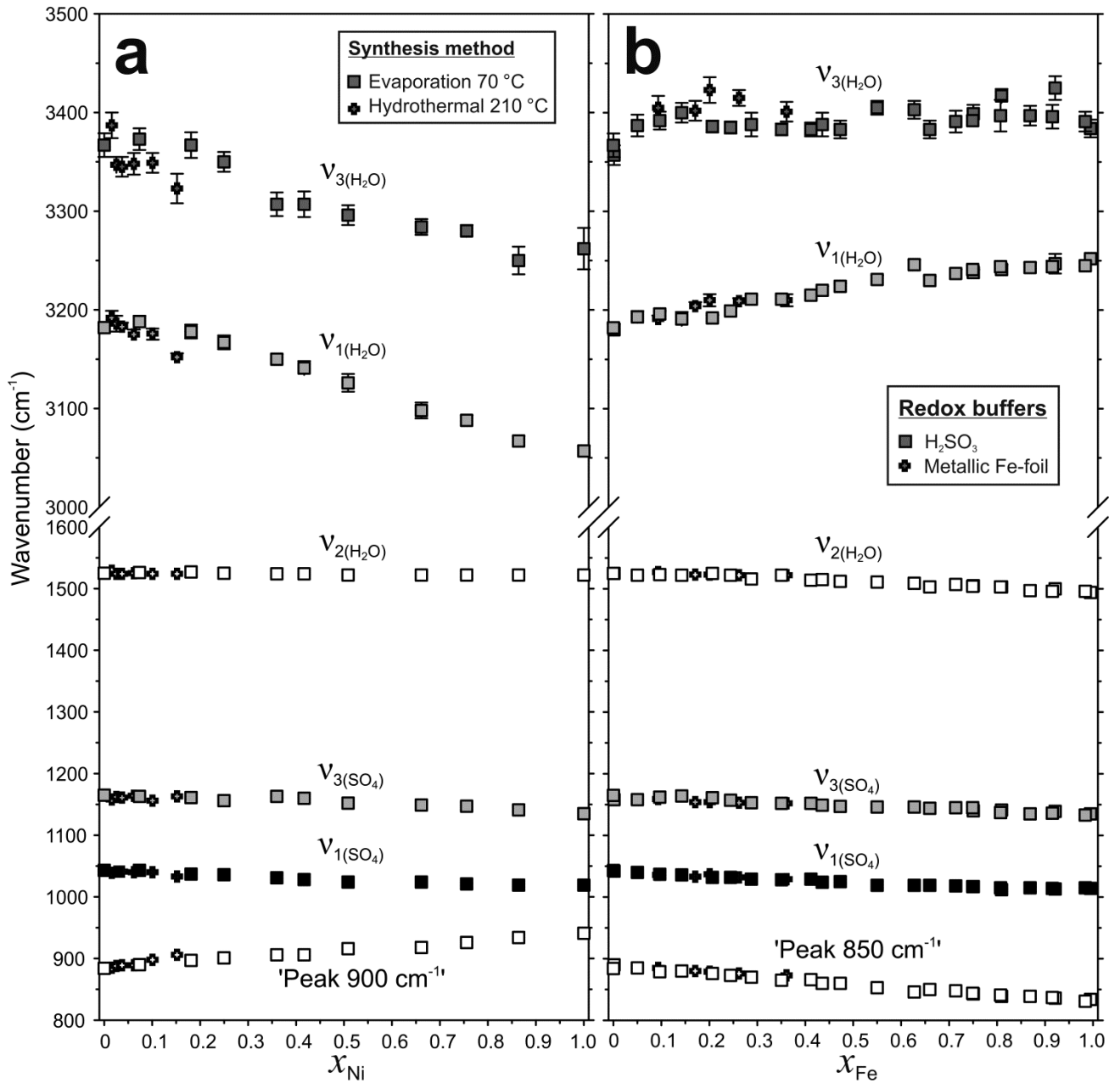
1264

1265

1266

1267

1268   **Figure 10.** Dependence of the FTIR absorption band positions of (**a**) the $Mg_{1-x}Ni_x(SO_4)\cdot H_2O$

1269   solid solution and (**b**) the $Mg_{1-x}Fe_x(SO_4)\cdot H_2O$ (**b**) on temperature, as seen in transmission

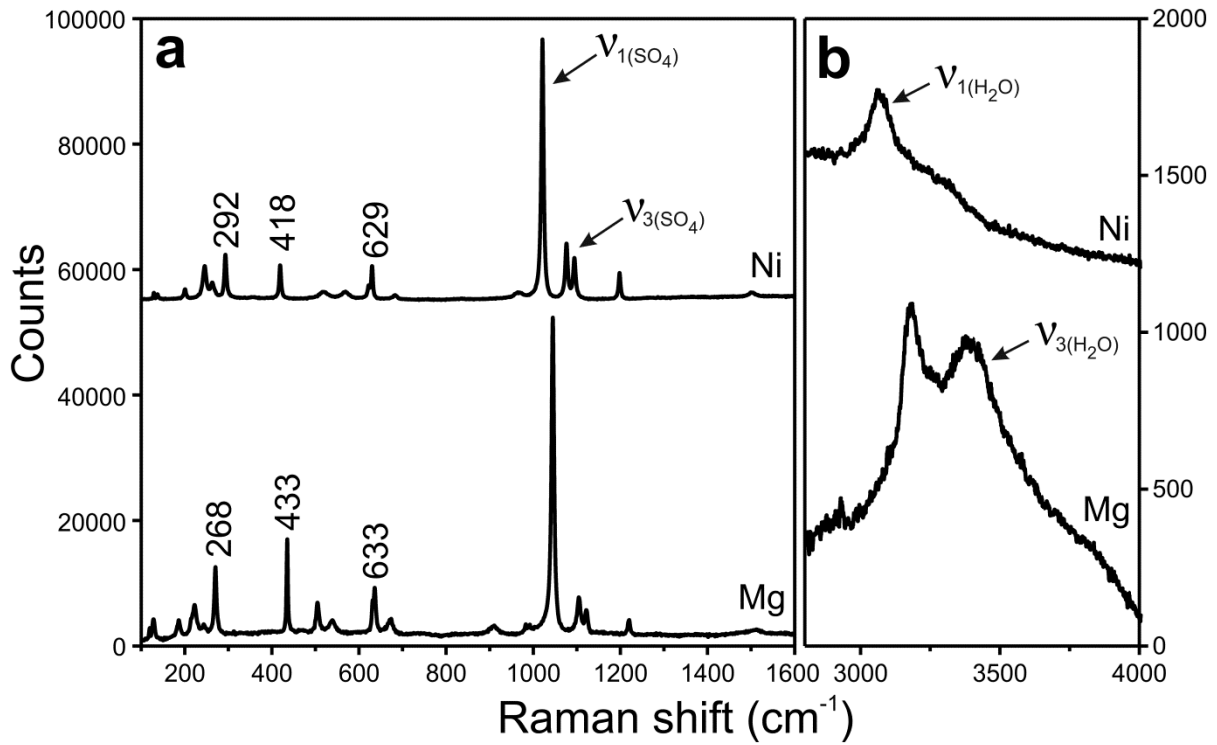1270   mode. Data for the Mg-Fe solid solution are taken from Talla and Wildner (2019).
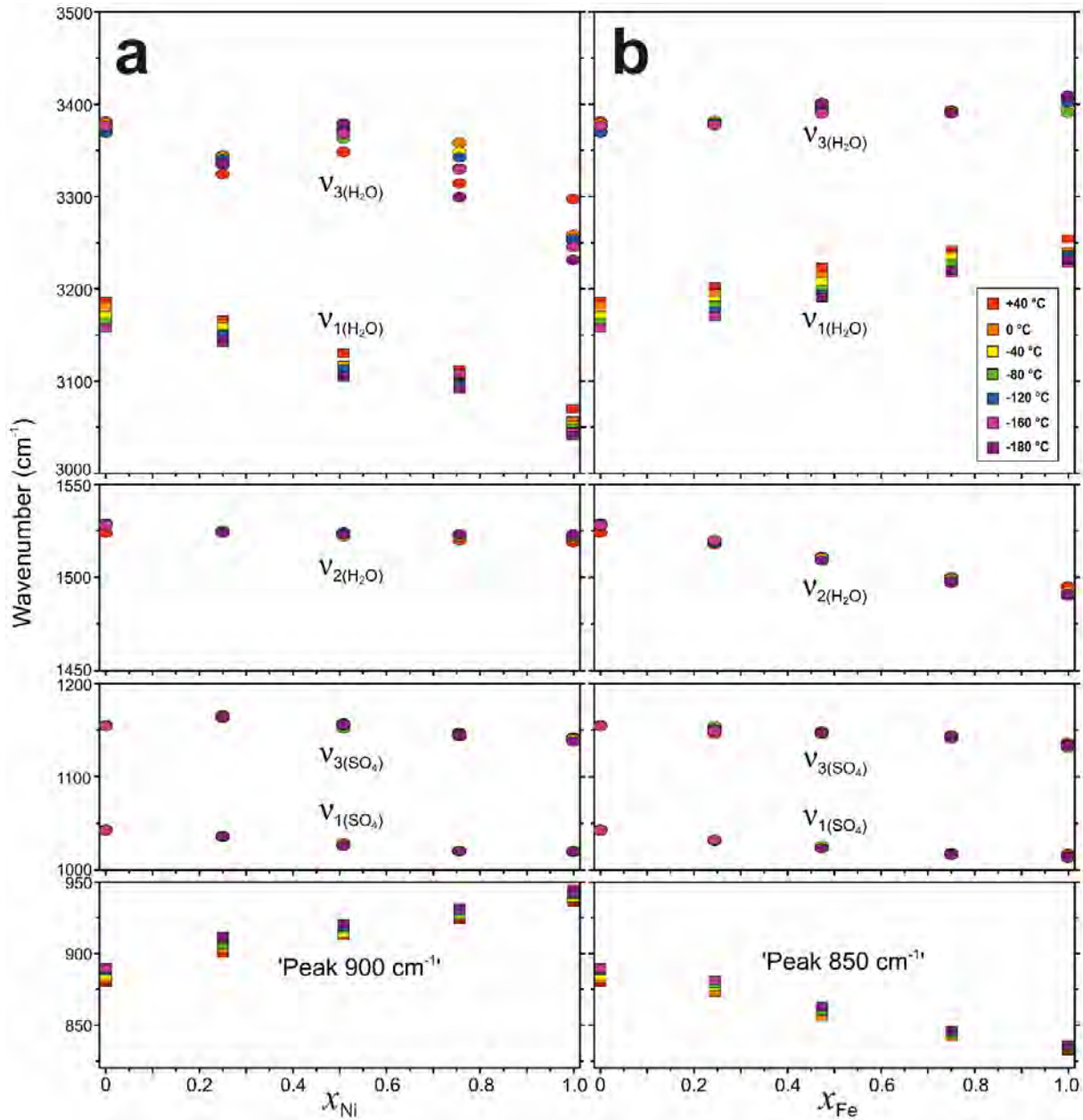

1271

1272

1273

1274

1275   **Figure 11.** Raman spectra of dwornikite (Ni) and kieserite (Mg) at room temperature in the

1276   region of (**a**) tetrahedral, octahedral and lattice modes, and (b) in the region of the O–H

1277   stretching modes. Data for kieserite are taken from Talla and Wildner (2019).

1278

1279

1280

1281

1282

1283

1284

1285

1286

1287

1288

1289

1290

1291

1292   **Figure 12.** Dependence of the Raman band positions in the $Mg_{1-x}Me_x(SO_4)\cdot H_2O$ solid

1293   solution series on (**a**) the Ni content and on (**b**) the Fe content at room temperature. Errors are

1294   equal or smaller than the symbol size. Data for the Mg-Fe solid solution are taken from Talla

1295   and Wildner (2019). Cross symbols in (**a**) differentiate between samples obtained

1296   hydrothermally with a fully sealed autoclave from those prepared by the evaporation

1297   technique (squares), while crosses in (**b**) discern the use of a metallic Fe redox buffer from
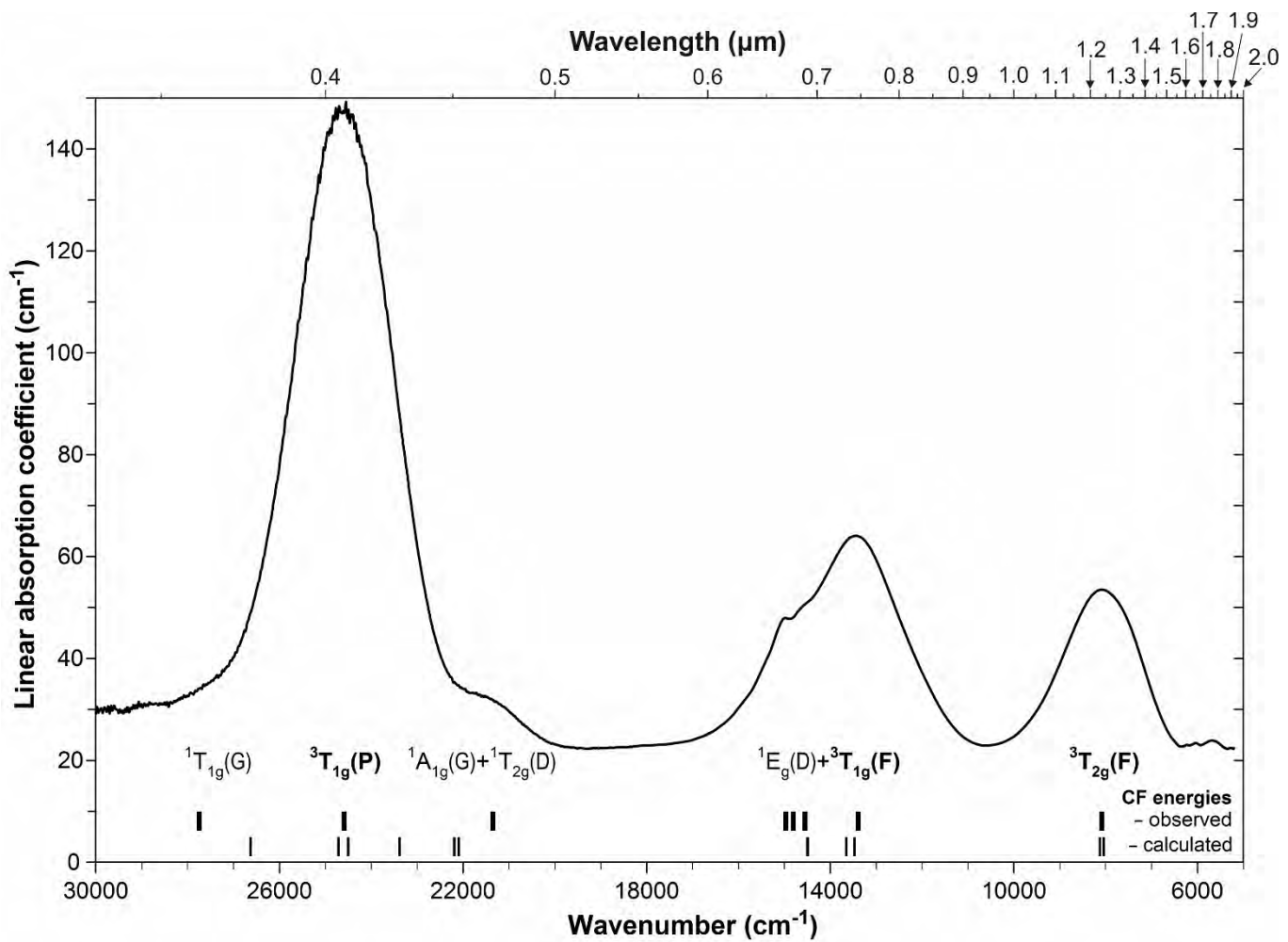
1298 H_2SO_3.
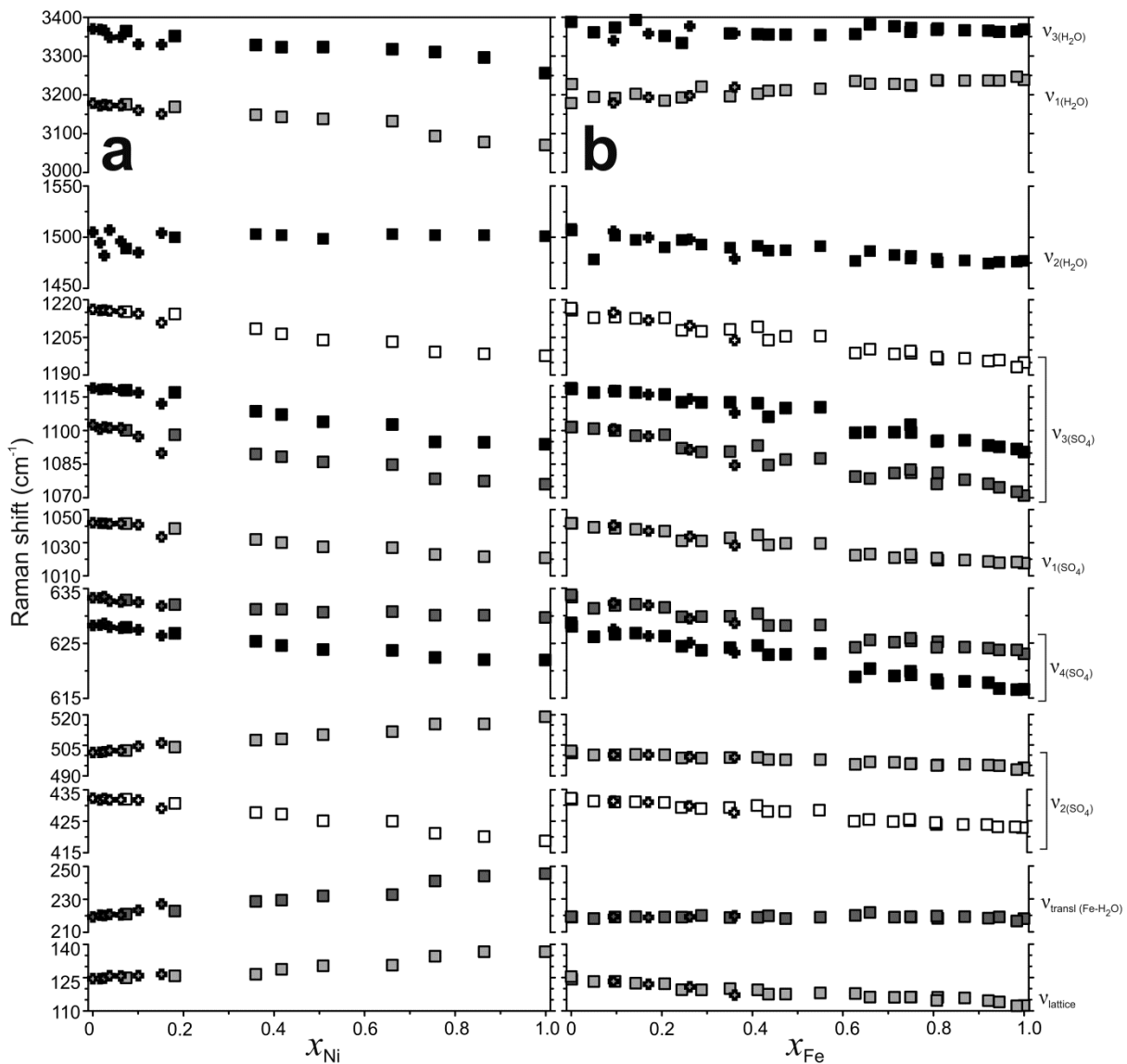
1299

1300

1301

1302

1303

1304

1305

1306   **Figure 13.** UV-Vis-NIR absorption spectrum of dwornikite in the range from 30000–5000

1307   cm^{-1} with observed (bold line marks) and calculated energy levels (thin line marks) and

1308   respective assignments for cubic symmetry.

1309

1310
1311